

# **Advances in MRI-based radiation therapy**

**Bringing MRI-only and multiparametric  
methods towards clinical applications**

Emilia Palmér

Department of Medical Radiation Sciences  
Institute of Clinical Sciences  
Sahlgrenska Academy, University of Gothenburg



UNIVERSITY OF GOTHENBURG

Gothenburg 2023

Cover illustration by Emilia Palmér

Advances in MRI-based radiation therapy - Bringing MRI-only and  
multiparametric methods towards clinical applications

© Emilia Palmér 2022  
emilia.palmer@gu.se

ISBN 978-91-8069-112-6 (PRINT)  
ISBN 978-91-8069-112-3 (PDF)

Printed in Borås, Sweden 2022  
Printed by Stema Specialtryck AB



”Inte varmt men nästan vår  
Ingen lösning men ett spår  
Inte ja men inte nej  
Inte bra men helt okej”

- Lars Winnerbäck



# Abstract

MRI data have the advantage of being excellent in soft tissue contrast, therefore having an increasing imaging role in external radiation therapy (RT). Lately, attention has been directed towards MRI-only workflows, with the approach of completely excluding the original CT data as a pre-treatment imaging modality. Instead, the RT workflow is based solely on MRI data. To access the electron densities needed for calculation of the absorbed dose distribution, synthetic CT data (sCT) are generated utilizing image processing or deep learning (DL) based methods. Besides purely anatomical information for guidance of a RT workflow, many functional and microstructural properties, such as cell density, microvascular structure, perfusion, and oxygenation of the tumor, could be highly relevant for RT treatment guidance and early RT assessment. It has been proven that hypoxia has an essential role in treatment outcome for HN cancer patients receiving radiation therapy. The potential to monitor hypoxia by functional and anatomical MRI (i.e., multiparametric MRI) is sparsely evaluated, and more studies are required to be able to establish robust MRI-derived hypoxia biomarkers.

The research within this thesis aimed to validate the MRI-only workflow for head and neck (HN) cancer, by evaluating sCT data generated by a nowadays commercially available DL-based method. The geometric and dosimetric properties were compared to the original CT data (Paper I), and as they were similar it was concluded that sCT can be used for dosimetric purposes. Further, both 2D and 3D patient setup verification based on sCT data was evaluated by comparison of the verification registrations with the registrations obtained when using the original CT data (Paper II). As the registrations for sCT and CT obtained similar patient positions, it was concluded that sCT data can be used for patient setup verification. As the generation of sCT data is based on complex models, a quality assurance (QA) process was developed to assess the quality of sCT data for prostate cancer (Paper III). A comparison between calculated absorbed dose distributions based on sCT and cone beam CT (CBCT) acquired for treatment setup verification, was shown to detect intentionally introduced errors within the sCT data. In addition, the research within this thesis aimed to implement and evaluate the potential of Oxygen-Enhanced (OE) MRI, intravoxel incoherent motion (IVIM), and diffusion kurtosis imaging (DKI) to monitor hypoxia, and their potential as useful tools for early response assessment in HN cancers (Paper IV). Each of these MRI pulse sequences was optimized and successfully implemented within a clinical RT setting. By comparing MRI-derived biomarkers acquired before and during RT for HN cancer patients, changes could be monitored during the course of

treatment. Further work regarding correlations of relative changes in these MR derived biomarkers to the treatment outcome is required to conclude the prediction value of OE-MRI and IVIM/DKI imaging for early response assessment.

The research presented in this thesis contributed to the clinical feasibility of MRI-only radiation therapy for multiple cancer types. In addition, the research showed that it is possible to implement multiparametric MRI for tumor characterization and treatment follow-up in the radiation therapy process for the complex HN region.

# Sammanfattning

Extern strålbehandling är en metod som används för att bekämpa cancer. Syftet med extern strålbehandling är att behandla tumörområdet och samtidigt skona omkringliggande känsliga organ. Ett viktigt steg vid planering av extern strålbehandling är att bestämma tumörens position i kroppen på ett så korrekt sätt som möjligt. Detta görs genom att studera anatomiska bilder och sedan i dessa bilder rita ut både tumören och de känsliga organen i närheten av tumören. Magnetkamerabildtagning (MR) har stor betydelse för utritning av tumörer eftersom den har god förmåga att visuellt särskilja olika mjukdelar i kroppen. MR kan även användas för att ta fram bilder som avspeglar biologiska egenskaper. Detta kallas för funktionell MR och kan spegla egenskaper som till exempel blodflöde. När både tumör och känsliga områden i kroppen har ritats ut i bilderna räknas det på hur strålbehandlingen ska genomföras. Till detta steg används röntgenbildtagning i form av datortomografi (DT eller den engelska förkortningen CT). En CT ger information om kroppens elektrondensitet vilket krävs för att man ska kunna beräkna hur strålbehandlingen ska levereras. CT används även vid varje behandlingstillfälle för att kontrollera att patientens kropp placeras likadant varje gång. Detta görs genom att använda sig utav ytterligare en bild ("cone-beam CT") som jämförs med CT-bilden.

På senare tid har ett nytt arbetssätt presenterats där enbart MR-bilder används för att planera strålbehandlingen. Att utesluta CT-bilder från behandlingsplaneringen minskar den totala stråldosen till patienten. Dessutom kompletteras oftast CT ändå med en MR-undersökning för att kunna definiera tumören tydligt i bilderna. Inom det nya arbetssättet krävs fortfarande information om elektrondensiteten i kroppen, som tidigare erhöles från CT-bilden. Därför används metoder för att omvandla MR-bilder till CT-liknande bilder (syntetisk CT) med hjälp av bildbehandling eller artificiell intelligens (AI). Användandet av AI inom medicin har visat sig vara ett bra verktyg och användningsområdena ökar konstant. Vid användning av AI inom strålbehandling och framtagande av nya arbetssätt är det viktigt att kontrollera att det nya arbetssättets resultat blir lika bra (eller bättre) som för det gamla arbetssättet. Detta för att säkerställa att det ges en minst lika bra behandling till patienten som tidigare.

Studierna i denna avhandling fokuserar kring användandet av syntetisk CT inom det nya arbetssättet där enbart MR-bilder används för att planera strålbehandling. Det undersöktes om syntetisk CT ger likvärdigt resultat som den traditionella CT-bilden när den användes för att räkna på hur

strålbehandlingen ska genomföras. Det undersöktes också om syntetisk CT ger lika resultat som den traditionella CT-bilden när den användes för att bekräfta att patientens kropp placeras likadant vid varje behandlingstillfälle. Dessa delarbeten har hjälpt till att visa att AI-baserad omvandling av MR-bilder till syntetiska CT-bilder är användbart inom strålbehandling. Vidare är det viktigt att säkerställa att omvandlingen från MR till syntetisk CT är korrekt varje gång. Därför utvecklades en metod som kontrollerade kvaliteten hos den syntetiska CT-bilden genom att jämföra den med "cone-beam CT". Vidare introducerades funktionell MR-bildtagning inom strålbehandling för att öka möjligheten att tidigt upptäcka hur patienten svarar på behandlingen. Metoder som har möjligheter att indirekt ge information om vävnadens syresättning, genomblödning och mikrostruktur infördes för huvud-halscancer. MR-bilder med funktionell information togs vid två tillfällen; en första gång innan behandling och en andra gång två veckor in i behandlingen. Jämförelse av bilderna från de två olika MR tillfällena visade vissa skillnader, men vidare undersökningar är nödvändiga för att ta reda på vad dessa skillnader i biologiska egenskaper betyder.

Forskningen som presenteras inom denna avhandling bidrog till möjligheten för kliniskt införande av MR-baserad strålbehandling. Den bidrog också till möjligheten att få tillgång till funktionell information för att tidigt uppdaga hur patienten svarar på behandlingen.



# List of papers

This thesis is based on the research presented in the following four studies, which are referred to in this thesis by their numerals.

- I.     **Synthetic computed tomography data allows for accurate absorbed dose calculations in a magnetic resonance imaging only workflow for head and neck radiotherapy**  
Palmér E, Karlsson A, Nordström F, Petruson K, Siverson C, Ljungberg M, Sohlín M.  
*Phys Imaging Radiat Oncol.* 2021;17:36-42
- II.    **Head and neck cancer patient positioning using synthetic CT data in MRI-only radiation therapy**  
Palmér E, Nordström F, Karlsson A, Petruson K, Ljungberg M, Sohlín M.  
*Journal of Applied Clinical Medical Physics.* 2022;23(4):e13525
- III.   **Cone beam CT for QA of synthetic CT in MRI only for prostate patients**  
Palmér E\*, Persson E\*, Ambolt P, Gustafsson C, Gunnlaugsson A, Olsson LE.  
\*Contributed equally to this study  
*Journal of Applied Clinical Medical Physics.* 2018;19(6):44-52
- IV.    **Oxygen-enhanced and intravoxel incoherent motion MRI for detection of radiation therapy induced changes of head and neck cancer**  
Palmér E, Brovall J, Jalnefjord O, Petruson K, Nordström F, Karlsson A, Ljungberg M, Sohlín M.  
*Manuscript*

# The author's contribution

- |           |  |
|-----------|--|
| Paper I   | The author participated in the study design and was responsible for the image processing, analysis, and interpretation of the results. The author was the main author of the paper.  |
| Paper II  | The author contributed significantly to the planning of the study and the data acquisition. The author was responsible for image processing and evaluation. The author was the main author of the paper.   |
| Paper III | The author was involved in the study design and contributed significantly to the data acquisition and analysis. The author contributed to writing the paper and shared the first authorship.   |
| Paper IV  | The author was responsible for the planning of the study and the data acquisition. The author contributed to the development of the image evaluation pipeline and was responsible for the analysis and interpretation of the results. The author wrote the manuscript. |

# Selection of related presentations

1. **Absorbed dose calculation based on CBCT data for head and neck cancer patients**

Palmér E, Sohlin M, Petruson K, Ljungberg M, Karlsson A  
*6th MR in RT Symposium 2018; Utrecht, Netherlands*

2. **Dosimetric evaluation of deep learning generated synthetic CT data for H&N MRI only radiotherapy**

Palmér E, Karlsson A, Nordström F, Siversson C, Petruson K, Ljungberg M, Sohlin M  
*ESTRO 2020; Vienna, Austria (Digital)*

3. **Treatment planning and quality control of an MRI only workflow for H&N patients using CNN based sCT**

Palmér E, Karlsson A, Nordström F, Petruson K, Ljungberg M, Sohlin M  
*8th MR in RT Symposium 2021; Heidelberg, Germany (Digital)*

4. **Promising results using synthetic CT for 2D and 3D patient positioning in head and neck radiotherapy**

Palmér E, Nordström F, Karlsson A, Petruson K, Ljungberg M, Sohlin M  
*ISMRM 2021; Vancouver, Canada (Digital)*

5. **Estimation and visualization of geometric fidelity using geometric offset maps for improved guidance in H&N radiation therapy**

Palmér E, Ljungberg M, Karlsson A, Nordström F, Petruson K, Sohlin M.  
*ISMRM 2022; London, United Kingdom*

6. **Oxygen-enhanced (OE) and intravoxel incoherent motion (IVIM) MRI for detection of radiation therapy induced changes in head and neck cancer**

Palmér E, Brovall J, Jalnefjord O, Petruson K, Nordström F, Karlsson A, Ljungberg M, Sohlin M.  
*9th MR in RT Symposium 2023; Los Angeles, United States of America*



# Abbreviations

|       |                                     |
|-------|-------------------------------------|
| ADC   | Apparent Diffusion Coefficient      |
| CBCT  | Cone Beam Computed Tomography       |
| CNN   | Convolutional Neural Network        |
| CT    | Computed Tomography                 |
| $D$   | Diffusion coefficient               |
| $D^*$ | pseudo-Diffusion coefficient        |
| DCE   | Dynamic Contrast Enhanced           |
| DKI   | Diffusion Kurtosis Imaging          |
| DRR   | Digitally Reconstructed Radiographs |
| DSC   | Dice Similarity Coefficient         |
| DWI   | Diffusion Weighted Imaging          |
| $f$   | perfusion fraction                  |
| HD    | Hausdorff Distance                  |
| HN    | Head and Neck                       |
| HU    | Hounsfield Units                    |
| IVIM  | IntraVoxel Incoherent Motion        |
| MAE   | Mean Absolute Error                 |
| ME    | Mean Error                          |
| MRI   | Magnetic Resonance Imaging          |
| OE    | Oxygen-Enhanced                     |

|       |   |
|-------|---|
| Oxy-E | Oxygen-Enhancing                              |
| Oxy-R | Oxygen-Refractory                             |
| QA    | Quality Assurance                             |
| $R_1$ | Relaxation rate                               |
| RT    | Radiation Therapy                             |
| sDRR  | synthetic Digitally Reconstructed Radiographs |
| sCT   | synthetic Computed Tomography                 |
| WED   | Water Equivalent Depth                        |

# Content

- Introduction ..... 1
- Aims ..... 3
- Magnetic resonance imaging in radiation therapy..... 5
  - The role of pre-treatment MRI in radiation therapy ..... 6
  - Considerations for implementation of pre-treatment MRI ..... 7
- Implementation of MRI-only ..... 11
  - Synthetic CT generation methods ..... 12
  - Treatment planning using synthetic CT data ..... 15
  - Patient setup verification using synthetic CT data..... 18
  - Quality assurance of synthetic CT data ..... 20
- Multiparametric magnetic resonance imaging in radiation therapy ..... 23
  - Tumor hypoxia..... 23
  - DCE MRI ..... 24
  - DWI, IVIM, and DKI MRI ..... 25
  - OE-MRI ..... 26
  - Radiation therapy treatment assessment using multiparametric MRI..... 27
  - Challenges of multiparametric MRI in radiation therapy ..... 32
- Conclusions ..... 35
- Future perspectives..... 37
- Acknowledgement..... 39
- References ..... 41





# Introduction

The number of new cancer cases and cancer deaths during 2020 has been estimated to be 19.3 million and 10 million cases respectively, where prostate cancer was the fifth leading cause of cancer death among men (375 000 deaths worldwide) and head and neck (HN) cancers combined were ranked ninth in cancer mortality overall (367 555 deaths worldwide)<sup>1</sup>. Most prostate and HN cancer patients undergo external beam radiation therapy (RT), with the purpose to deliver a sufficiently high absorbed dose of ionizing radiation to the tumor to control disease, while limiting the absorbed dose to surrounding healthy tissue for minimal radiation toxicity. Control of the absorbed dose to the tumor and surrounding healthy tissue during RT is crucial and require high geometric accuracy throughout treatment preparation and daily setup of the patient at the treatment device. In order to reach the full potential of RT, there is an increasing demand for functional and anatomical imaging techniques<sup>2</sup>, and ideally, functional tools for treatment monitoring and early response assessment.

At present, computed tomography (CT) is the gold standard imaging modality, constituting the basis for the entire RT treatment course<sup>3</sup>. This imaging modality provides the correlation between Hounsfield units (HU) and the electron densities necessary for absorbed dose calculation during treatment planning. Magnetic resonance imaging (MRI) is a non-ionizing imaging modality with multiple and superior soft tissue contrasts compared to CT. Due to its excellent soft tissue contrast, MRI is established as the preferred imaging modality for contouring tumor and organs at risk (OAR) during treatment planning where a precise definition is needed<sup>4</sup>. Due to the increasing role of MRI in RT, attention has been directed towards RT planning using MRI data solely, often referred to as an MRI-only workflow. The MRI-only workflow aims to reform the treatment preparation process by completely excluding CT data from the RT course, resulting in the elimination of both multiple patient imaging sessions and the otherwise required MR to CT registration<sup>5</sup>. However, the gap of nonexistent electron density information in the MRI data must be bridged in order to implement a complete MRI-only workflow. One suggested solution is to convert MRI data to so-called synthetic CT data (sCT), having the same physical characteristics as CT data. Various approaches for sCT generation have been proposed<sup>6-8</sup> and require validation against the original CT before MRI-only workflows can be safely implemented in the clinic.

Besides providing anatomical information, MRI offers functional imaging methods that reflect functional and microstructural information of biological

tissue<sup>9</sup>. In addition to the anatomical image-based MRI-only workflow for improvement of the accuracy of the RT workflow, the combination of functional and anatomical MRI techniques (i.e., multiparametric MRI) increases the information available for treatment response assessment at follow-up, and potentially also during the treatment course. Relative changes of MRI derived functional and microstructural information during treatment might be a predictor of treatment response and long-term outcome and hence act as a non-invasive tool for individualized RT<sup>10</sup>. A potential marker for early treatment response assessment is tumor tissue hypoxia, a comparatively fast-changing condition known to cause resistance of the tumor to RT treatment<sup>11,12</sup>.

Within the research presented in this thesis, numerous steps within the MRI-only workflow have been explored. Treatment planning (Paper I) and patient setup verification (Paper II) were validated using a commercial sCT generation method (MriPlanner). Since the sCT generation is technically challenging and standardized quality assurance (QA) programs have not yet been established, an independent QA method to detect potential errors in the generated sCT using cone beam CT was investigated (Paper III). In addition, the functional MRI techniques Oxygen-Enhanced (OE) MRI, intravoxel incoherent motion (IVIM), and diffusion kurtosis imaging (DKI) was implemented to monitor hypoxia changes during the course of HN treatment (Paper IV).

# Aims

This thesis aimed to evaluate and validate MRI-only prostate and head and neck radiation therapy as well as implement and evaluate the feasibility of multiparametric head and neck MRI in radiation therapy, with the ultimate goal to improve the clinical feasibility of MRI in radiation therapy.

The specific aims of the papers included in this thesis were:

- to validate the geometric and dosimetric accuracy of MRI-only head and neck cancer treatment planning when based on a commercial deep learning-based synthetic CT generation method (Paper I)
- to validate MRI-only head and neck patient setup verification when based on a commercial deep learning-based synthetic CT generation method (Paper II)
- to develop and evaluate a quality assurance method for synthetic CT data in MRI-only prostate radiation therapy (Paper III)
- to implement and evaluate the feasibility of using Oxygen-Enhanced MRI, intravoxel incoherent motion, and diffusion kurtosis imaging for early response assessment in head and neck cancers (Paper IV)



# Magnetic resonance imaging in radiation therapy

There were 19.3 million new cancer cases reported worldwide in 2020, where prostate cancer was ranked the third most commonly diagnosed cancer (1 414 259 cases), and HN cancers combined were ranked as the eighth (747 316 cases). In addition, prostate cancer was the fifth leading cause of cancer death among men (375 000 deaths worldwide) while HN cancers combined were ranked ninth in cancer mortality overall (367 555 deaths worldwide)<sup>1</sup>. In high-income countries, mortality rates have decreased for prostate cancer since the mid-1990s, probably a reflection of the advances in treatments and increased screening for earlier detection. However, high-resource countries now have signaled a stabilization in the prostate mortality decline<sup>1</sup>. External beam radiation therapy (RT) is a common treatment method for both prostate and HN cancer. The advances in RT towards 3D treatment methods, such as intensity-modulated RT (IMRT) and volumetric-modulated arc therapy (VMAT), have resulted in conformal treatment plans. A prerequisite for the introduction of 3D treatment methods was the transition from 2D to 3D imaging<sup>13</sup>, offering more information about the target volume and surrounding healthy tissue. The advanced 3D RT courses used today include numerous steps, i.e., immobilization of the patient in RT position, pre-treatment imaging (e.g., CT, MRI, and/or positron emission tomography (PET)), contouring of treatment volume and organs at risk (OAR), treatment planning, patient-specific quality assurance (QA), treatment delivery, and patient follow-up.

During contouring, the radiation oncologist delineates the tumor as the gross target volume (GTV). Before treatment planning, a margin is added to the GTV to assure inclusion of undistinguishable subclinical spread of disease, creating the clinical target volume (CTV). To account for uncertainties within the RT course and ensure coverage of the CTV, an additional margin is added generating the planning target volume (PTV) (figure 1). The delineation of the treatment volume has been identified as the weakest link within the RT course<sup>14</sup>, and as this step relies on high geometric accuracy of the pre-treatment image data that serve as a basis for the contouring, these data are an essential component for optimal treatment delivery. The increasing demand for precise contouring of treatment volume and OARs has brought the introduction of pre-treatment MRI in RT about, as this modality provides multiple and increased contrast information compared to the traditional CT data, which depends only on the attenuation of x-rays within tissue, measured in Hounsfield Units (HU).

## The role of pre-treatment MRI in radiation therapy

The current gold standard image basis for RT workflows is CT data. In CT data, tissues with considerably different HU (e.g., air, soft tissue, and bone) can be readily distinguished, while there are difficulties in differentiating soft tissues with similar HU (e.g., tumor and adjacent soft tissue) (figure 1). MRI is a non-ionizing imaging modality that can produce images with many different anatomical contrasts (e.g., T1-weighted, T2-weighted, and PD-weighted) by altering different basic pulse sequence parameters (e.g., repetition time (TR), echo time (TE), and flip angle ( $\alpha$ )). The most commonly used MRI contrasts within RT are T1- and T2-weighting (figure 1), which provide complementary anatomical information as different tissues possess different T1 and T2 relaxation time properties. This flexibility in creating contrast in MR images improves the ability to distinguish both between adjacent soft tissues with similar electron densities and tissue with considerably different electron densities. Further, acquisition of MR images can be conducted in any oblique planes, which may improve the delineation of the target boundary in the cranio-caudal direction compared to CT data that is limited to axial acquisition.

By introduction of MRI during contouring, and with that enhanced contrast visibility of tumors, OARs, and their boundaries, the target volumes for RT have been shown to increase for brain cancer<sup>15,16</sup> while decreasing for prostate<sup>17-19</sup> and HN cancer<sup>19-21</sup>. A change in defined target volume by the introduction of MRI data into the RT course indicates that the use of CT alone for delineation of targets may underestimate or overestimate the target volume. In addition to the image quality, the accuracy of the target delineation is also dependent on the expertise and training of the physician. There are no general guidelines regarding volume delineation for RT, causing a vast variability in delineation within and between radiation oncologists. Introduction of MRI data during delineation led to smaller interobserver differences for volumes outlined on MRI than on CT data for brain<sup>16,22</sup>, prostate<sup>23</sup>, and HN<sup>24</sup> cancer. In addition to anatomical information, MRI may also provide functional and microstructural information by implementation of enhanced MRI sequences such as diffusion-weighted imaging (DWI) and dynamic contrast-enhanced (DCE) MRI, representing incoherent water molecular motions and blood flow respectively. These noninvasive functional MR techniques map tumor functions in their entirety, as opposed to the regionally limited tissue

information available via biopsy, and might be able to identify distinct target regions that would benefit from an absorbed dose boost during treatment<sup>25,26</sup>.

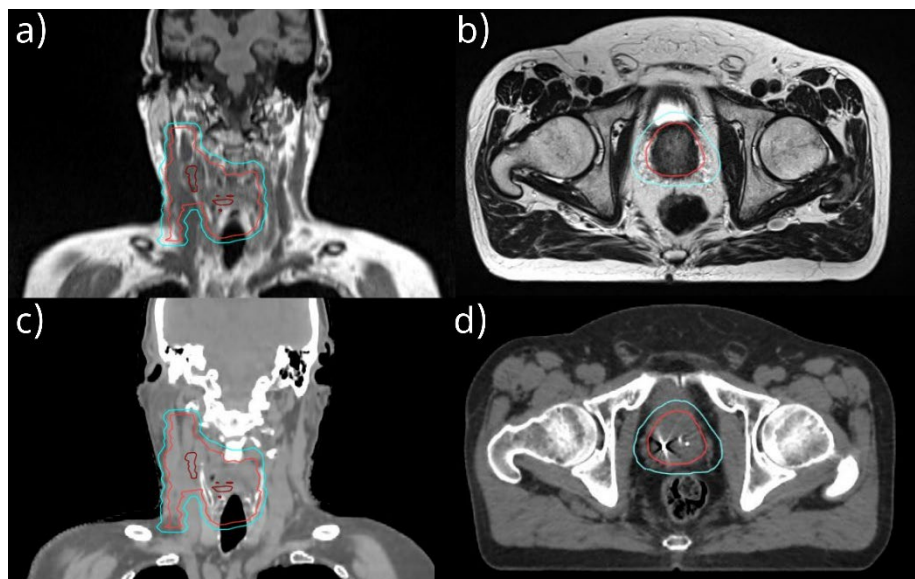


Figure 1. a) T1-weighted head and neck (HN) magnetic resonance image (MRI), b) T2-weighted prostate MRI, and c-d) corresponding computed tomography (CT) images. Delineated are gross target volume in HN (dark red), clinical target volume (light red), and planning target volume (light blue).

## Considerations for implementation of pre-treatment MRI

In the standard multi-modality RT course, pre-treatment MRI data are registered to a planning CT, hence allowing for MRI-based delineation together with CT-based treatment planning. To achieve a high-quality inter-modality registration, it is desirable to have identical patient positioning during both imaging sessions, as well as identical patient external and internal geometry. This, however, is unachievable, and the existing differences will impact the quality of the MR to CT registration. To mitigate the registration errors by avoiding large differences in the patient geometry, both data sets are preferably acquired in close time to each other. In addition, to obtain as identical patient RT position as possible, MRI scanners dedicated to RT should preferably be equipped with an indexed flat tabletop, MRI-compatible patient immobilization devices, coil bridge supports, and external lasers for alignment. All these adaptations constitute MRI signal challenges and ultimately impact the image quality, e.g., the immobilization devices used for brain and HN cancer require a wide-bore MRI scanner and prevent the use of high-

performance receiver coils, leaving the user to less efficient flexible phased array coils. In addition, to preserve the outer body contour for not immobilized cancer patients (e.g., prostate cancer), the flexible coils are mounted on coil bridges, adding an air gap between the patient and the receiver coils. An alternative, recently presented by GE Healthcare (Chicago, Illinois, USA), is the lightweight flexible air coils as they should be light enough to preserve the patient outer body contour. Furthermore, the use of immobilization devices during MRI causes additional patient discomfort, and the scanning session should therefore consist of carefully selected sequences to limit the total scan time.

In comparison to diagnostic MRI, MR images used in RT have higher demand on geometric accuracy as they are used for precise contouring of tumor and OAR, and therefore will affect the amount of healthy tissue that is irradiated. The sources of geometric distortion in the MRI data can be separated into two components, i.e., system-dependent, and patient-dependent distortions. The main contribution of system-dependent distortions is nonlinear gradient fields, disturbing the spatial encoding and causing the origin of the MRI signals to be mislocated, which makes the reconstructed images spatially distorted. The magnitude of the distortions is typically negligible within a small field of view (FOV) at the MR-system isocenter but increases with increasing distance from the isocenter. As MRI in RT often requires large FOV, quantification of the geometric distortions by a QA process utilizing a phantom object is essential. However, system-dependent geometric distortions have been extensively evaluated and vendor-supplied algorithms are available to reduce the geometric distortions to clinically accepted levels, although not completely removed<sup>27,28</sup>. Patient-dependent distortions arise as a result of the magnetic properties of the patient, i.e., different magnetic susceptibility for different tissues within the body. Unlike system-dependent geometric distortions, patient-related geometric distortions are difficult to predict since the magnetic properties of two patients are not the same, and therefore more difficult to correct for<sup>28</sup>. To generate pre-treatment MRI data with high geometric accuracy, MR images used in RT are typically acquired with higher readout bandwidth compared to diagnostic imaging, at the expense of a lower signal-to-noise ratio.

Although thriving towards both identical patient positioning for the imaging modalities and high MRI geometric accuracy, geometric uncertainties related to the MR-CT registration will still be present<sup>29-34</sup>. There are numerous causes for this, such as imperfect registration algorithms, as well as internal body movements (e.g., breathing, or intestinal motions) which are hard to correct for during the imaging sessions. These geometrical uncertainties will introduce a



systematic error during the treatment planning stage, affecting each treatment fraction, and propagating through the entire treatment course. The added PTV margin has accounted for these (and other) uncertainties, ensuring coverage of the clinical target volume during the whole RT course.



# Implementation of MRI-only

*This chapter is mainly related to Paper I, Paper II, and Paper III.*

*In Paper I, acquired HN data was used to validate treatment planning for synthetic CT data (sCT) in an HN MRI-only workflow by comparing geometrical and absorbed dose differences between sCT and original CT data. Acquisition of training HN data contributed to the development of the used deep learning (DL) based sCT generation algorithm.*

*In Paper II, methods to compare sCT-based treatment setup verification to CT-based treatment positioning for HN MRI-only workflow were developed and evaluated.*

*In Paper III, a method for quality assurance (QA) of a hybrid-based generated sCT was presented and evaluated for a prostate MRI-only workflow.*

The most common clinical integration of MRI in RT is as a secondary source of information, used for delineation and co-registered towards the planning CT. MRI data, however, have potential of being the primary source of information and used for both delineation and treatment planning. This is often referred to as the MRI-only workflow and has the approach of completely excluding the CT as a pre-treatment imaging modality. In such workflow, all preparation steps are then carried out using MRI data solely, hence eliminating the MR to CT registration and, with this, also the correlated systematic geometric uncertainties that otherwise propagate throughout the entire treatment workflow. In addition, the reduction of the number of imaging sessions in the MRI-only workflow eases the patient's discomfort, especially for those immobilized in RT position as well as for young pediatric patients that avoid multiple anesthetics.

Before implementing an MRI-only workflow in the clinic, development and validation of methods allowing for both treatment planning and treatment setup verification are essential. In addition, it is necessary to estimate the impact on delineation when using MRI data as the only imaging modality, together with the impact of MRI geometric distortions propagating to treatment planning. Finally, procedures for QA in the MRI-only treatment planning process must be established as there are no CT data available for evaluation. To date, few centers worldwide have implemented, and treated patients, in an MRI-only workflow<sup>35-39</sup>.

## Synthetic CT generation methods

The absorbed dose calculation performed during the treatment planning process requires electron density information for the anatomical area of interest. CT data inherently possess electron density information as it derives from the attenuation of x-rays within the tissue. MRI data have no such direct relationship to electron density, but several methods have been proposed to generate so-called synthetic CT data (sCT) (also called pseudo-CT, substitute-CT, or virtual-CT) based on MRI data that would enable absorbed dose calculation and patient setup verification within an MRI-only workflow. The general concept of sCT generation is creation of data that resembles CT data, i.e., that has the same physical characteristics (HU-values) as CT data, but with the additional benefit of being generated directly in the MRI frame of reference (FoR). Current methods to generate sCT data either rely on tissue information available in the MRI data (voxel-based), are built on conversion methods relying on the correlation between paired MRI-CT data sets (atlas-based), or are based on deep learning<sup>40</sup>. Synthetic CT has been developed and evaluated for multiple treatment regions, but most extensively for the brain and pelvis (prostate) regions.

### *Voxel-based sCT generation*

Voxel-based methods for sCT generation are built on tissue classification, mainly by segmentation of the MRI data into classes depending on signal intensity of each voxel and subsequent assignment of a homogenous electron density value to each class<sup>6-8,40</sup>. The simplest approach is to define only one tissue class and assign the HU value of water within the entire body contour. Such homogeneous methods have the advantage of very fast sCT generation but at the cost of absent bone structures needed for treatment setup verification. More advanced methods utilize multiple tissue classifications (e.g., bone, air, and soft tissues), creating a more heterogeneous sCT by manual contouring or (semi)auto-segmentation of the tissues in CT or MRI data<sup>6,7,41,42</sup>. An issue of multiple tissue classification-based methods is the difficulty to separate air and bone tissues in standard MRI pulse sequences, as the short T2\* relaxation time of bone tissue will lead to low signal values which can be mistaken as the signal void caused by air. Hence, time-consuming manual bone or air contouring is often necessary which is not practical for clinical use<sup>7</sup>. Another approach for separation of bone and air in MRI is the utilization of ultrashort echo-time (UTE)<sup>7,8,42</sup> or zero echo-time (ZTE)<sup>42</sup> pulse sequences to generate sCT data, either as the sole pulse sequence or in combination with other standard MRI pulse sequences<sup>6,7</sup>. Additional voxel-based techniques to generate sCT data utilize statistical methods, such as clustering or regression models<sup>6-8,42</sup>. A

benefit of voxel-based methods to generate sCT data is the robustness towards atypical anatomy, but with the disadvantage of often requiring multiple pulse sequences.

### *Atlas and patch-based sCT generation*

Atlas-based methods rely on the correlation between matching MR and CT images, where an atlas consists of one or more co-registered MRI and CT pairs. For creation of sCT data, the MRI data in the atlas are typically registered to the incoming MRI data, generating transformation matrixes and deformation fields that are applied to the CT, hence generating a corresponding sCT data set<sup>6-8,40,42,43</sup>. If an atlas consists of multiple pairs, one approach is to register the MR data sets within the atlas, creating an average MRI data set and a corresponding average CT data set. Another approach is to contain the data in the atlas separated and register each atlas MR data set to the incoming MRI data followed by fusing of the propagated atlas CT data sets (e.g., voxel patch comparison). The advantage of atlas and extended patch-based sCT data generation is its dependence on only one single standard MRI pulse sequence, although the large number of registrations makes it time-consuming, and it is also insensitive to atypical anatomy within the patient MRI data.

### *Hybrid-based sCT generation*

The introduction of hybrid-based methods to generate sCT data combines multiple generation methods to take advantage of the benefits of the different generation methods. One proposed hybrid-based method utilizes a statistical decomposition algorithm (SDA)<sup>44</sup> (used in Paper III), which combines tissue segmentation with a multi-atlas-based approach to generate sCT data. In a prostate cancer example, this method auto-segmentate the prostate, bladder, colon, bones, and fat structures in the incoming MRI. The segmentation is followed by a nonlinear warping procedure, where a deformable registration algorithm aligns each segmented structure in the atlas with the automatically segmented structures. Subsequently, linear deformations are applied to the atlas data, both within and between the structures, followed by a constrained deformation to align fine-grained structures of each deformed MRI within the atlas to the incoming MRI. The resulting deformation fields are then applied to the corresponding CT data of each atlas case, finally generating a sCT data set by voxel-wise calculation of the weighted median HU value<sup>44</sup>.

*Deep learning-based sCT generation*

Deep learning (DL) methods for sCT data generation are based on neural networks trained on the relationship between MRI signal intensities and HU values<sup>40,45</sup>. The currently foremost used DL-based sCT generation strategy is the generator-only model convolutional neural network (CNN)<sup>45</sup>, consisting of an input layer, multiple hidden layers, and an output layer<sup>40,45</sup>. The hidden layers within the CNN convolve the input matrix with trainable convolutions kernels, generating a feature map passed to the next layer. The input matrix is restricted by an activation function, defining the output of the layer given an input, where the most common function is the nonlinear activation function ReLU (rectified linear units)<sup>40,46</sup>. In addition, batch normalization (i.e., rescaling of the input to a standard distribution), as well as dropout layers, are commonly applied to obtain a robust and fast convergence of the model and to reduce the probability of overfitting, respectively<sup>46</sup>. To reduce the number of trainable parameters and the amount of computer memory needed, insertion of pooling layers in between layers, down-sampling the feature maps by dividing the data into rectangular pooling regions, and calculating for example the maximum of each region (max-pooling) is commonly used<sup>40,43,46</sup>. The aim of the CNN training is to minimize an objective function called a loss function<sup>40,45,46</sup>, which in sCT generation is an intensity-based similarity measurement between the generated sCT and the corresponding ground truth CT data<sup>40</sup>. The training consists of iterative adjustments on the kernel weights until a minimized loss function is achieved<sup>46</sup>. Once the training session is completed, the sCT generation can be validated by comparing sCT data with independent CT data, not included in the training data set. A proposed DL-based method to generate sCT data is the so-called transfer function estimation (TSE) algorithm<sup>47</sup> (used in Papers I and II). The TSE algorithm generates spatially variant coefficients of an affine transfer function utilizing deep CNNs which are fed to the transfer function and applied to the incoming MRI, generating the sCT data. The TSE algorithm consists of several 3D CNNs with multiple convolutional layers and residual connections (also called skip connections). The TSE algorithm used in Papers I and II was trained using a multi-center database with paired MRI and CT datasets that were augmented during training<sup>47</sup>. The benefit of DL-based sCT generation is the fast generation. However, as the training of the CNN is based on a training data set, the quality of the output from the CNN depends on the quality of the training data as well as the similarity between the input MR and training data.

### *Commercial sCT generation methods*

The TSE algorithm is a commercially available solution, presented within MriPlanner<sup>47</sup> (Spectronic Medical AB, Helsingborg, Sweden). There are several additional commercially available solutions for sCT generation utilizing different generation methods, simplifying the standardization of the MRI-only workflow. Multiple tissue classification methods such as MRCAT<sup>48,49</sup> (Philips Healthcare, Cleveland, OH, USA) and Synthetic CT solution in RT image suite<sup>50,51</sup> (Siemens Healthcare, Erlangen, Germany) are examples of previously presented solutions. There are also hybrid-based generation methods such as the SDA via MriPlanner<sup>44,52</sup> (Spectronic Medical AB, Helsingborg, Sweden), as well as DL-based generation methods such as Synthetic CT solution in RT image suite<sup>53</sup> (Siemens Healthcare, Erlangen, Germany).

## Treatment planning using synthetic CT data

In the traditional RT workflow, the acquired planning CT data are imported into the treatment planning system. The CT data in combination with the delineated structures are then used to plan the delivery of the treatment radiation beam by tracking and modulating the absorbed dose distribution using certain calculation algorithms. In an MRI-only workflow, the sCT will instead be used as the calculation base throughout the treatment planning process. Currently, extensive evaluations of the geometric and dosimetric accuracy of generated sCT data as the basis for RT treatment planning have been conducted<sup>7,8,40,45,46,54</sup>. The most common metrics used within the evaluation of dosimetric agreement are the gamma pass rate, the relative point dose differences, and dose-volume histograms (DVH) comparisons<sup>6,42,43</sup>. For evaluation of the geometrical agreement, common metrics are the mean absolute error (MAE) and the Dice similarity coefficient (DSC)<sup>6</sup>. The MAE here describes the absolute voxel-wise difference in HU between sCT and CT data and is defined as

$$MAE = \frac{1}{n} \sum_{i=1}^n |sCT_i - CT_i|$$

where  $n$  is the number of segment voxels. The MAE estimates the magnitude of the HU difference between the imaging sets while over- or underestimation of HU-values is not estimated. The DSC evaluates the similarity between the segmented volumes in the sCT and CT data, defined as

$$DSC = \frac{2|V_{CT} \cap V_{sCT}|}{|V_{CT}| + |V_{sCT}|}$$

where  $|V_{CT}|$  and  $|V_{sCT}|$  are the binary masks of the segmented structure in CT and sCT data, respectively, and  $|V_{CT} \cap V_{sCT}|$  the volume of their intersection. A DSC value of 1 represents perfectly overlapping structures and a value of 0 no overlap at all. DSC calculated for small structures can be sensitive to HU generation errors as it depends on the size of the structures. It is noteworthy that all the metrics described here are not directly comparable between studies, as different studies are designed with e.g., unrelated absorbed dose calculation algorithms and different threshold values for bone segmentation.

Treatment plans based on sCT data generated using homogeneous water-equivalence methods resulted in acceptable dosimetric agreement compared to CT-based treatment plans for both prostate and brain<sup>6,7,41</sup>. However, treatment plans where the beam passed through internal air (e.g., for HN and thorax) obtained nonacceptable dosimetric disagreement<sup>7,41</sup>. The introduction of multiple tissue classifications for sCT generation improved the dosimetric agreement compared to single bulk-density assignment<sup>7,8</sup>. The hybrid-based method to generate sCT data used in Paper III has been dosimetrically validated in a multi-center multi-vendor study for prostate cancer patients<sup>52</sup>. The conclusion was that the sCT-based absorbed dose distributions were similar to those based on CT data, and in line with previously published results for atlas- and voxel-based sCT generation methods<sup>6,7</sup>.

In Paper I, the reliability of DL-based sCT generation for HN treatment planning was evaluated by comparing the geometrical and absorbed dose differences between sCT and original CT data<sup>55</sup>. The HN sCT data were generated using a pre-released version of a now commercially available DL-based method utilizing a TSE algorithm (MriPlanner) (figure 2). The dosimetric agreement between sCT and CT data was evaluated by analyzing gamma pass rates and relative local absorbed dose differences for a subset of DVH parameters. The original CT dose plan was recalculated on sCT data using identical beam parameters, resulting in a mean absorbed dose difference range from -0.3% to 0.02% for all DVH parameters. The 3D gamma evaluation (2%/1 mm criteria) presented a 99.4% mean gamma passing rate for sCT against CT dose distributions. The results from the dosimetric evaluation were in line with previously presented DL-based sCT generation methods within the HN region<sup>56-59</sup>. Extensive metrics were presented to evaluate the geometrical agreement, i.e., the difference in mean error (ME) and MAE, DSC, and Hausdorff distance (HD) for overall body, soft tissue, bone, and air segments.



The ME here describes the voxel-wise difference in HU between sCT and CT, defined as

$$ME = \frac{1}{n} \sum_{i=1}^n sCT_i - CT_i$$

The ME evaluation enables detection of over- or undergenerated HU values within a tissue segmentation. The HD describes the similarity between the segmented volumes in the sCT and CT data, resulting in an estimation of the distance between the respective tissue segments in sCT and CT, defined as

$$HD(A, B) = \max(h(A, B), h(B, A))$$

with

$$h(A, B) = \max_{a \in A} \min_{b \in B} \|a - b\|$$

where  $h(A, B)$  is the directed HD from surface structure voxels in CT data  $A$  to the surface structure voxels in sCT data  $B$ . Intuitively,  $h(A, B)$  identifies voxel  $a$  in  $A$  as the furthest from any voxel in  $B$  and measures the distance from  $a$  to the nearest neighbor in  $B$ . Further, each voxel in  $A$  is ranked based on the distance to the nearest neighbor in  $B$  where the largest ranked voxel and corresponding distance is the directed HD<sup>60</sup>. Finally,  $HD(A, B)$  is the maximum of  $h(A, B)$  and  $h(B, A)$ . As HD depends on the maximum value, it is sensitive to HU generations errors. The difference in water equivalent depth (WED) between sCT and CT data was also presented, defined as

$$WED = \sum_i \Delta d_i \rho_i$$

where  $\Delta d_i$  is the physical photon distances of voxel  $i$  to isocenter and  $\rho_i$  is the electron density, i.e., WED represents both geometric and dosimetric properties<sup>6</sup>. The results from the geometrical evaluation of the generated sCTs were comparable to previously published DL-based HN data<sup>56-59,61-63</sup>. The study concluded that the utilized TSE algorithm generates sCT data suitable for absorbed dose calculations in an MRI-only workflow for HN RT. At the time, only a small number of studies had focused on HN DL sCT generation<sup>40</sup>. Paper I in this thesis presented and evaluated a nowadays commercially available and CE-approved DL-based sCT generation method, increasing the clinical accessibility to MRI-only HN RT compared to in-house developed DL-based generation methods previously published.

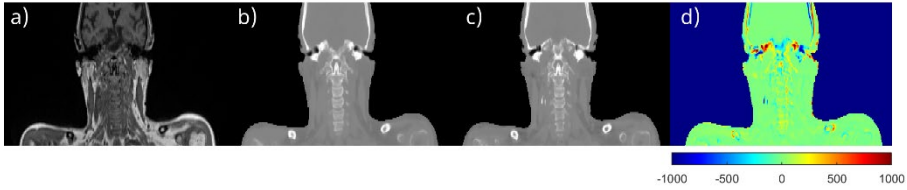


Figure 2. a) Magnetic resonance image (MRI), b) deep learning-based generation of synthetic computed tomography (sCT), c) computed tomography (CT) data, and d) the corresponding difference (sCT-CT) in Hounsfield units (HU). The largest differences in HU can be seen around the ear canals, an area sensitive to susceptibility effects.

## Patient setup verification using synthetic CT data

To ensure that a linear accelerator delivers geometrically correct RT to the patient, daily imaging is performed at the treatment machine. Using these images, the anatomy of the patient is adjusted to match the patient position employed during pre-treatment imaging for absorbed dose planning. This adjustment is achieved by registration of the daily images to the reference image used for treatment planning, followed by an adjustment of the treatment couch according to the obtained translation and rotation differences. Usually, 2D orthogonal x-ray images are acquired and registered with digitally reconstructed radiographs (DRR) originating from the planning CT (figure 3). The 2D orthogonal x-ray images depicture bony anatomy well but have almost no soft tissue visualization. The introduction of 3D cone beam CT (CBCT) on the treatment machine allowed for 3D visualization of both bony anatomy and soft tissue and can be registered directly to the planning CT, allowing for 3D patient setup verification (figure 3). Once patient setup is adequately verified, the daily RT absorbed dose can be delivered. In an MRI-only workflow, where the sCT is the basis for treatment planning, patient setup verification is performed by registering the 2D orthogonal x-ray images with synthetic DRR (sDRR) and 3D CBCT with the sCT, respectively (figure 3).

Recently, extensive evaluations have demonstrated promising results for the dosimetric performance of generated sCT data, whereas the accuracy and precision of treatment setup verification utilizing sCT data have been less reported<sup>5,46</sup>. It could therefore be argued that more attention and validation should be directed toward other steps in the MRI-only workflow than the dosimetric accuracy, such as treatment setup verification using sDRR or sCT data. As homogeneous water-equivalent methods to generate sCT data have no information about bony structures, treatment setup verification using such sDRRs is not possible. However, as the methods for sCT generation were refined, these structures become available and some studies have validated

bone-based treatment setup verification using sDRR and/or sCT for different treatment sites and generation methods<sup>48,64-69</sup>. Only a few studies have investigated HN sCT-based treatment setup verification<sup>57</sup> and DL-based sCT generation methods are in general sparsely reported for all anatomical regions<sup>39,57,70,71</sup>. The few numbers of available publications focusing on HN patient setup verification might be a result of the heterogeneity in tissue structures and complex freedom of motion for this anatomical region. Paper II aimed to evaluate the use of sCT and sDRR for patient setup verification in HN RT for the now commercially available TSE algorithm (MriPlanner)<sup>72</sup>. Here, the metrics used to evaluate treatment setup verification were DSC together with translation and rotation differences for a reference point between sCT/sDRR and the original CT/DRR. The methodology is presented in figure 3. The 2D manual and 3D automatic registration techniques used in the study were the same techniques used for treatment setup verification in the clinical setting. In addition, for easy interpretation and illustration of combined translation and rotation differences, the Euclidean distance was presented. The mean translation and rotation differences between CT and sCT-based treatment setup verification found were  $<0.7\text{mm}$  and  $<0.3^\circ$  in all directions for both 2D and 3D setup verification. The translational differences using 2D orthogonal projections were in line with previously presented studies evaluating patient setup verification for HN cancer<sup>57</sup>. As there were no previously published data for 3D patient setup verification in the HN region available, these results were related to and showed to be in line with other anatomical sites<sup>65,66,68,69,71</sup>. Paper II in this thesis showed that the utilized commercially available DL-based method generates sCTs that can be used as a reference for both 2D and 3D MRI-only treatment setup verification for the complex HN anatomy.

Same coordinate system

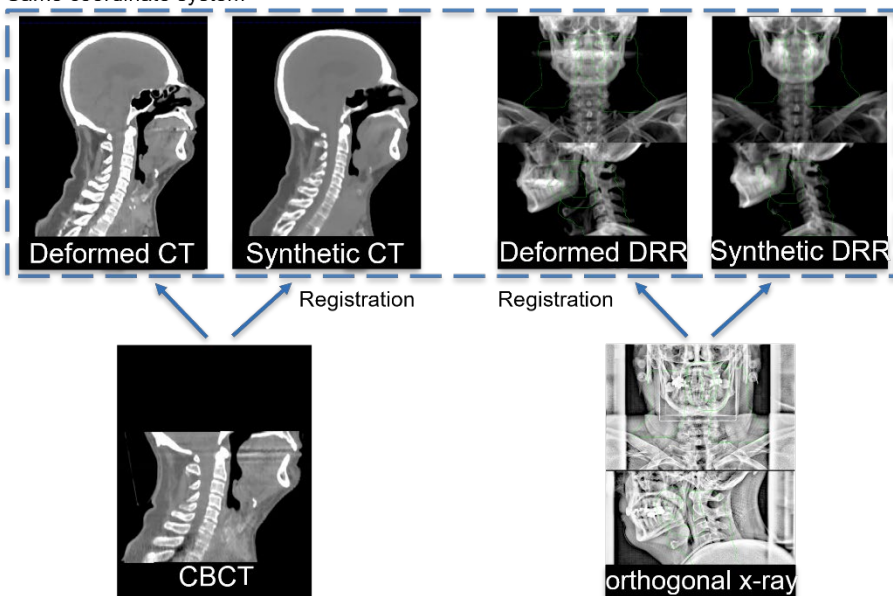


Figure 3. The methodology for Paper II. The digitally reconstructed radiographs (DRR) and the synthetic DRR originate from the planning computed tomography (CT) and synthetic CT, respectively. The 2D manual and 3D automatic registration techniques used in the study were the same techniques used for treatment setup verification in the clinical setting.

## Quality assurance of synthetic CT data

As MRI-only workflows are not yet routinely used and are considered new technology, implementation of such a workflow in a clinic setting requires QA<sup>73</sup>, and as the workflow removes the CT from the pre-treatment imaging session there is no sCT/CT comparison available to assure the accuracy of the generated sCT data. As the generation of sCT data incorporates complex models and is not fully transparent when utilizing DL-based models, there might be scenarios where generation errors are introduced within the sCT data. In addition to technical circumstances, errors might occur due to other conditions such as accidental changes in the MRI pulse sequence parameters related to the sCT generation, or atypical patient anatomy or artifacts not included in the generation models. The generated sCT data can be visually inspected to detect potential errors, however, the introduction of an independent tool for QA of the sCT data would be desirable<sup>68,69</sup>, preferably before or in close connection to the start of RT. One QA approach is to use a secondary independent sCT generation method<sup>73,74</sup>. An additional approach is to use the fact that both the sCT and CBCT data, acquired for treatment setup

verification, consist of HU-values. This enables a comparison of the attenuation information from the two modalities and has been suggested as an independent patient-specific QA<sup>68,69</sup>. This method could be further extended to evaluate also the dosimetric differences between the sCT-based dose distribution and a recalculated CBCT dose distribution, which has been presented for prostate<sup>75</sup> (Paper III), HN<sup>76</sup> (presented abstract no.1), and brain<sup>77</sup> cancer patients. The evaluations for prostate and HN concluded that a simple recalculation of the dose distribution using CBCT data acquired at the first treatment fraction is comparable to the dose distributions for CT as well as sCT data. The sCT generation method for prostate was the SDA (MriPlanner) and for HN an early version of the TSE algorithm (MriPlanner). The prostate study also introduced simple artificial errors within the sCT data to demonstrate the feasibility of the method to flag unacceptable sCT generation errors for clinical use, although, suggesting an action level requires a more extensive evaluation. A study evaluating CBCT-based QA for DL-generated sCT data of the brain proposed two action levels: a 3% absorbed dose difference with corrective action applied before the next fraction and a 2% absorbed dose difference with the corrective action applied within the next three fractions<sup>77</sup>. Such suggested levels need to be considered for other tumor sites, and possibly tailored for a specific clinical site before being implemented. Paper III in this thesis concluded that CBCT data can be used as a tool for QA to detect gross errors within the sCT generation in MRI-only RT, and as CBCT imaging is a routinely used imaging technique for treatment setup verification it constitutes a clinically practical tool for QA in MRI-only workflows without introduction of new imaging sessions.

High geometric accuracy for MRI in RT is desirable and achieved by carefully designed MRI sequences. In an implemented MRI-only workflow, no CT data are available to monitor the MRI data. In addition, as sCT data are generated from the MRI, any geometric distortions in the MRI data will propagate to the sCT data, and hence affect the entire RT course. For this reason, characterization of the geometric distortions for each sequence used in an MRI-only workflow is necessary<sup>5</sup>. Previous studies have evaluated the impact of geometric distortions on the dosimetric distribution for MRI pulse sequences used for sCT-generation and concluded that the geometric distortions have a minor dosimetric impact<sup>78,79</sup> except for whole-breast RT<sup>27</sup>. As the geometric distortion varies between pulse sequences and MRI systems, they should be quantified for any MRI pulse sequence used for sCT generation before MRI-only workflow implementation. The MRI pulse sequences used to generate sCT in Papers I, II, and III showed negligible system-depended geometric distortions<sup>80,81</sup>. Further analysis regarding patient-related geometric distortions is needed and is proposed to be conducted by calculation of field distortion

maps<sup>82</sup> (presented abstract no.5) from the dual-echo T1-weighted Dixon data used to generate HN sCT data in Papers I and II. As the geometric distortion may vary over time, it would be desirable to measure the geometric distortions for the MRI pulse sequence used for sCT generation, preferably integrated into the clinical quality control (QC) of the MRI system<sup>73</sup>.

# Multiparametric magnetic resonance imaging in radiation therapy

*This chapter is mainly related to Paper IV.*

*In Paper IV, methods to acquire OE-MRI and IVIM/DKI MRI for HN cancer were developed. The feasibility of these techniques was evaluated regarding their potential use as an early treatment assessment tool for HN radiation therapy.*

As mentioned, in addition to anatomical information, MRI can also provide functional and microstructural information through implementation of advanced MRI sequences such as DCE, DWI, and OE-MRI. Besides purely anatomical information for guidance of an RT workflow, many functional and microstructural properties, such as cell density, microvascular structure, perfusion, and oxygenation of the tissue, could be highly relevant for RT treatment guidance<sup>9,26,83</sup> as it increases the information available for assessment of treatment response at follow-up and potentially also during the treatment course<sup>9,83</sup>. However, a combination of functional and anatomical MRI techniques (multiparametric MRI) is currently not routinely used in a clinical RT setting, as rigorous quantification and validation of the methods are still required<sup>9,83</sup>.

## Tumor hypoxia

Tumor hypoxia arises due to an imbalance between the tumor oxygen supply and demand, which depends on the extent of tissue perfusion together with the oxygen consumption of the tumor cells<sup>84</sup>. Inadequate and heterogeneous oxygen supply often found in tumor tissue is caused by numerous factors such as limitation in diffusion distance of oxygen through tissue (chronic hypoxia), and reduced tissue perfusion due to temporary closing of tumor blood vessels caused by malformed vasculature (acute hypoxia)<sup>85,86</sup>. It has been shown that cells are more sensitive to x-ray radiation in the presence of molecular oxygen compared to under hypoxia<sup>86</sup>. As the presence of tumor hypoxia could affect the treatment outcome following RT, this measure has become an interesting factor to consider regarding treatment response, and correlations have been observed between hypoxia and angiogenesis, tumor aggressiveness, local recurrence, and metastasis<sup>11</sup>.

There are invasive techniques available to identify hypoxia, e.g., Eppendorf measurements and immunohistochemical staining<sup>11,12</sup>, which have been used

to associate tumor hypoxia with poor survival prognosis for HN cancer patients treated with RT<sup>87</sup>. In addition, promising investigations have been published evaluating hypoxia using positron emission tomography (PET)<sup>11,12,88</sup>, where <sup>18</sup>F-labeled fluoro-misonidazole (<sup>18</sup>F-FMISO) probably is the most extensively used PET imaging agent for hypoxia<sup>11</sup>. By repeated acquisition of <sup>18</sup>F-FMISO PET data for HN cancer patients during the RT course, it was shown that the reoxygenation for HN cancer starts early (approximately within 1-2 weeks) and that hypoxia is correlated to the treatment outcome<sup>89-91</sup>. Another approach for non-invasive assessment of hypoxia could be utilization of functional MRI techniques, which potentially even would be able to provide spatial mapping of hypoxic subregions in individual whole tumors<sup>11,12</sup>. Tissue hypoxia is a consequence of inadequate oxygen supply to the tumor tissue, caused by, for example, impaired diffusion and reduced tissue perfusion. This makes functional MRI techniques like DCE, IVIM, DKI, and OE-MRI (described below) promising tools for monitoring tumor characteristics causing hypoxia and, with that, allow for earlier RT treatment response assessment.

## DCE MRI

DCE-MRI is a conventional perfusion technique that relies on intravenous injection of a gadolinium (Gd) based contrast agent (CA) and builds on dynamic T1-weighted MR imaging before, during, and after the CA injection<sup>92</sup>. As the Gd-CA is paramagnetic, the signal of the dynamic DCE-MRI increases with CA accumulation due to a T1-shortening effect<sup>92</sup>. After CA injection, an initial concentration increase is observed for all tissue types, usually followed by a washout (decreased concentration) of the CA from the tissue. The Gd-CA immediately inhabits the blood plasma and is assumed to passively diffuse across the inner cellular lining of veins and capillaries and the tissue extracellular extravascular space (ESS). The CA diffusion depends on the volume transfer constant between blood plasma and ESS ( $K_{trans}$ ) and the rate constant between ESS and blood plasma ( $k_{ep}$ ). As Gd-CA does not enter cells, the CA concentration also depends on the fractional volume of blood plasma ( $v_p$ ) and the fractional volume of ESS ( $v_e$ ). Hence, the change in CA concentration over time depends on the volume fractions of the tissue compartments and physiological microvascular properties such as blood flow and capillary leakage<sup>92</sup>. DCE-MRI is often preceded by a quantitative T1 measurement (T1-mapping), allowing for a model-based quantification of  $K_{trans}$ ,  $k_{ep}$ ,  $v_e$ , and  $v_p$ . For patients with contraindications for CAs, or planned for multiple perfusion MRI examinations, the extended DWI MRI model denoted intravoxel incoherent motion (IVIM) is an interesting alternative to the traditional DCE MRI for perfusion estimation as it does not require an intravenous injection of CA.



## DWI, IVIM, and DKI MRI

The conventional DWI-MRI signal is sensitive to incoherent water molecular motions (e.g., diffusion), where the signal strength decays as a function of the amount of diffusion-weighting applied (described by the so-called b-value). By obtaining at least two DWI images with different b-values the average magnitude of diffusion for a voxel can be quantified, i.e., the metric apparent diffusion coefficient (ADC) can be calculated<sup>93</sup>. Tissue with high cell density (e.g., malignant tumor) characteristically restricts water diffusion, and as ADC is inversely proportional to the tissue cell density<sup>94</sup> malignant tumors have lower ADC-values compared to benign tumors which often have lower cell density<sup>95-98</sup>.

The more complex diffusion model IVIM MRI includes both tissue water diffusion and blood microcirculation (perfusion)<sup>99</sup>. In a tissue voxel, both water diffusion and perfusion are present, where the perfusion mimics a fast diffusion process and, hence, also impacts the DWI measurement<sup>100</sup>. The IVIM MRI technique separates these two physical phenomena without contrast agent involvement, quantifying tissue microstructural and vascular-specific characteristics such as diffusion of water ( $D$ ), diffusion of water in the blood ( $D^*$ ), and capillary perfusion fraction ( $f$ ) in the voxel<sup>99</sup>. IVIM MRI requires acquisitions of at least four DWI measurements with different b-values followed by a fitting of the IVIM model to the acquired data

$$S_b = S_0 \left( (1 - f)e^{-bD} + fe^{-bD^*} \right)$$

where  $S_b$  is the acquired signal at a specific b-value and  $S_0$  is the signal without diffusion weighting. The fitting process of the equation above has been shown to be sensitive to noise and may inaccurately estimate the IVIM parameters<sup>101</sup>. A simplified IVIM model, without estimation of the pseudo diffusion coefficient ( $D^*$ ), can be used if only estimates of the perfusion fraction ( $f$ ) and diffusion coefficient ( $D$ ) are of interest. This model is described as

$$S_b = S_0 \left( (1 - f)e^{-bD} + f\delta(b) \right)$$

where  $\delta(b)$  is the discrete delta function where  $\delta(b = 0) = 1$  and  $\delta(b \neq 0) = 0$ . The simplified IVIM model assumes that the signal loss with increasing b-value caused by  $D^*$  is fast compared to the signal loss due to  $D$  ( $D^* \gg D$ ), and hence, the signal intensities used to estimate the IVIM parameters are where  $e^{-bD^*}$  is either 1 ( $b = 0$  s/mm<sup>2</sup>) or negligible ( $b \geq$  than an assessed tissue-specific b-value threshold)<sup>102</sup>. The simplified IVIM is a faster method

regarding measurement time since fewer b-values are required when  $D^*$  is not estimated.

The simplified IVIM model is eligible for a two-step (segmented) fitting process. In a first step, an assumption that the signal contribution from the perfusion compartment is negligible for high b-values is made, which makes it possible to use a monoexponential diffusion model expressed as

$$S_b = Ae^{-bD} \quad b > b_{\text{threshold}}$$

In a second step,  $f$  is estimated as  $f = 1 - A/S_0$  where  $S_0$  is the signal intensity at  $b = 0$ . The benefit of segmented fitting is the robustness with less variability and hence fewer potential calculation errors<sup>101,103</sup>. The determination of the b-value threshold at which pure diffusion is assumed is a crucial part of the segmented fitting process, and no general value can be used as this depends on the biological characteristics of the evaluated tissue type<sup>101</sup>.

The IVIM model can be further extended by incorporation of the diffusional variance effects<sup>104,105</sup>. In previous models, the diffusion displacement probability distribution is assumed to have a Gaussian shape, however, the introduction of strong diffusion weighting (high b-values) causes the distribution to deviate from a Gaussian shape due to the complexity of various tissue structures (e.g., cellular compartments and membranes)<sup>104</sup>. The deviation from a Gaussian distribution can be determined by the kurtosis model, often denoted as diffusion kurtosis imaging (DKI)<sup>104,105</sup>, described as

$$S_b = S_0((1 - f)e^{-bD + \frac{1}{6}b^2D^2K} + f\delta(b))$$

where  $K$  is the kurtosis effect which represents the degree of non-Gaussian diffusion<sup>105</sup>.

## OE-MRI

An additional proposed method for mapping and quantification of tumor hypoxia is OE-MRI, also denoted Tissue Oxygenation Level Dependent (TOLD) MRI<sup>12</sup>. This MR imaging technique is based on quantification of temporal changes in the longitudinal relaxation rate ( $\Delta R_1$ ) during inhalation of oxygen ( $O_2$ ). These changes in  $R_1$  caused by the paramagnetic  $O_2$  can be assessed by dynamic acquisition of  $T_1$  maps (where  $R_1 = 1/T_1$ ) while breathing air (baseline) and while breathing 100%  $O_2$  and calculation of the difference between the two maps as per

$$\Delta R_1(t) = R_1(t) - R_1(0)$$

where  $R_1(t)$  is the relaxation rate at time  $t$  after switching to 100%  $O_2$  breathing and  $R_1(0)$  is the relaxation rate at baseline breathing air. In theory, a  $T_1$ -shortening would be found for well-oxygenated tissue while breathing 100%  $O_2$ , caused by an excess of dissolved paramagnetic  $O_2$  molecules in the blood plasma and surrounding interstitial space, resulting in a positive  $\Delta R_1$  (oxygen-enhancing (Oxy-E) voxels). However, in hypoxic tissue, the excess of  $O_2$  molecules during 100%  $O_2$  breathing binds to the unsaturated deoxyhemoglobin (Hb) molecules, leaving only a few dissolved  $O_2$  molecules in the tissue and thus resulting in a  $\Delta R_1$  close to zero<sup>12</sup>. The latter is also expected for necrotic tissue, as it is non-perfused. In order to distinguish between hypoxic and necrotic tissue it is suggested to utilize the difference in perfusion between the tissues. By combining data from OE-MRI and DCE-MRI measurements, tumor hypoxia can be identified as tissue that is oxygen refractory while still being perfused (perfused Oxy-R)<sup>106</sup>.

## Radiation therapy treatment assessment using multiparametric MRI

To date, the most common method to assess the treatment effect of RT for solid tumors is to measure the tumor size reduction within anatomical images (RESIST)<sup>107</sup>. However, as tumor size changes are a late effect these evaluations often take place several months after completed treatment and are therefore not suitable for treatment adaptations. It would be highly advantageous for earlier treatment assessment to identify non-responsive HN patients based on pre-treatment multiparametric MRI or early treatment-induced changes during RT. The information from pre- or mid-treatment multiparametric MRI could further also enable individual adaptation of the treatment<sup>88</sup>. However, few MRI-derived biomarkers have yet been adopted for clinical use. There is a critical need to develop quantitative imaging for RT purposes and evaluate the potential of these biomarkers for early response assessment, preferably with large study cohorts and external validation of the derived biomarkers<sup>9,83</sup>.

In paper IV, MRI pulse sequences were optimized for estimation of imaging biomarkers from IVIM/DKI and OE-MRI for RT of HN tumors. These MRI sequences were acquired before RT delivery and during RT (approximately 2 weeks of delivered RT) for evaluation of their potential as a tool for early guidance of RT treatment response assessment. The post-processing was conducted using an evaluation pipeline, where all data (except DWI) was

registered to the T1-weighted image acquired within the baseline OE-MRI sequence (figure 4).

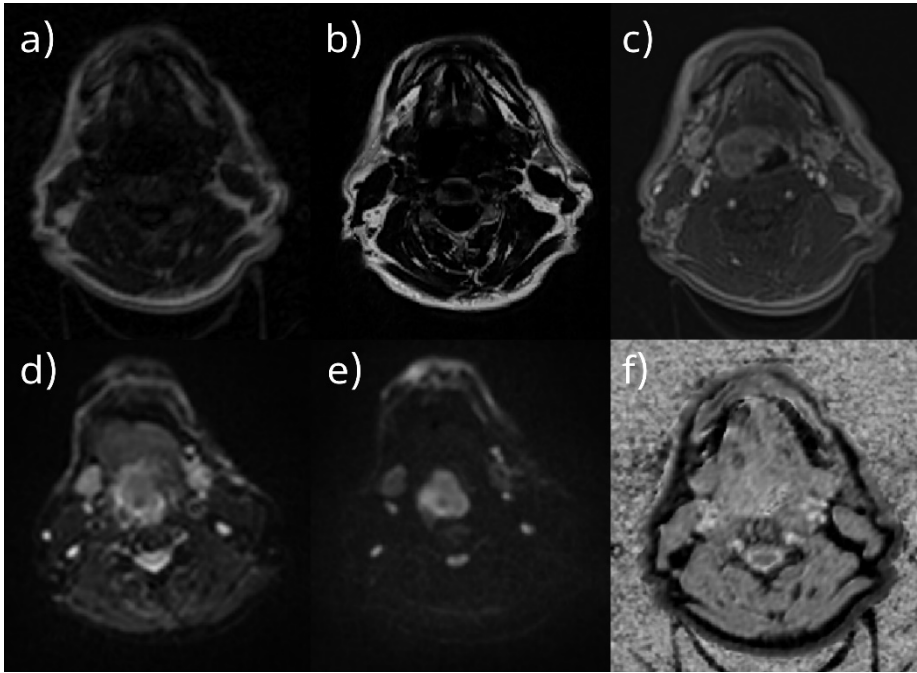


*Figure 4. A subset of anatomical and functional magnetic resonance imaging (MRI) techniques acquired within paper IV. a) T1-weighted MRI acquired within the baseline Oxygen-Enhanced (OE) MRI sequence, b) water-suppressed T2-weighted Dixon MRI image, c) dynamic contrast-enhanced MRI data at 30 seconds after gadolinium-contrast agent injection, d) diffusion-weighted imaging (DWI) data at  $b=0$  s/mm<sup>2</sup>, e) DWI data at  $b=1500$  s/mm<sup>2</sup> and f) calculated T1-map at OE-MRI baseline.*

#### *IVIM and DKI MRI*

The conventional DWI-MRI metric ADC has shown potential as a quantitative imaging biomarker to predict treatment outcome for HN cancer, where tumors with lower pre-treatment ADC values correlated with favorable treatment outcome<sup>108-110</sup>. Regarding characterization of early treatment response using mid-RT imaging, a larger increase in ADC values has been observed for tumors with encouraging treatment response<sup>95,110</sup>. An increase in ADC value following RT indicates changes within the extracellular and/or intercellular space, however, the underlying biological mechanisms of the increased water diffusion are hard to interpret since ADC is sensitive to many aspects of the tissue microstructure.

The IVIM/DKI model is more complex than the conventional ADC model and since it is sensitive to both water diffusion within tissue, blood microcirculation, and the degree of non-Gaussian diffusion, it has the potential to separate a larger number of tissue transformations. The IVIM/DKI model was applied in paper IV where DWI-MRI data were successfully acquired for all enrolled study cases, using a single shot echo planar imaging (ssEPI) sequence with four b-values ( $b = 0, 110, 650, \text{ and } 1500 \text{ s/mm}^2$ , number of repeated acquisitions = 1, 2, 3, 2). It has been suggested that careful optimization of b-values and the number of repeated acquisitions of each b-value minimize the uncertainties during estimation of  $D$  and  $f$ <sup>111</sup>. Within Paper IV, the b-values and number of repeated acquisitions per b-value were optimized using a framework previously presented by Jalnefjord et al.<sup>111</sup>, now extended to also include  $K$  in the optimization. The ranges of expected  $D$ ,  $f$ ,  $D^*$ , and  $K$  for various HN cancers were obtained from available literature<sup>112-118</sup>. From the optimization process, a b-value scheme for DWI data can be determined via error propagation and bias estimation for subsequent determination of the IVIM parameters with the segmented fitting process. As both error propagation and bias estimation is utilized, the b-value threshold for pure diffusion can be established as the lowest non-zero b-value (i.e.,  $110 \text{ s/mm}^2$  in this study). However, numerous things impact the specified IVIM parameters ranges and subsequently the optimized b-value scheme and b-value threshold. If the optimized b-value threshold is set too low, it would cause the  $D$ -values to be overestimated and the  $f$ -values to be underestimated. However, the ranges of  $D$ ,  $f$ ,  $D^*$  obtained from literature and used in the optimization could be of variable quality as the number of studies reporting IVIM parameters is sparse for HN cancer, the methods for parameter estimation are varying, the HN cancer type is a heterogenous group with multiple sub-cancer types, and study patients were both HPV positive and negative.

The IVIM/DKI parameters evaluated in paper IV were  $D$ ,  $f$ , and  $K$ , where an increase of  $D$  and  $f$  between imaging sessions indicates an increase in the mobility of water and microvascular blood volume, and a decrease in  $K$  implies a progression towards reduced microstructural heterogeneity. Four study cases out of seven had IVIM/DKI parameters with this changing pattern, indicating a positive treatment outcome<sup>112</sup>. Previously reported changes in tumor mean  $f$ -values before and during RT show various patterns, as both increasing<sup>112,118,119</sup> and decreasing<sup>120</sup> changes for positive treatment outcomes have been observed. For negative treatment outcomes, both increasing<sup>119</sup> and decreasing<sup>112,118,120</sup> changes were similarly observed. Inconsistent results for  $f$ -values changes following RT have been presented in the relatively few studies published, which might be due to numerous reasons, such as heterogeneous and HPV-positive or negative HN cancer types, different MRI measurement methods as

well as differences in signal modeling methodology. This emphasizes the need for further evaluation of how to interpret IVIM-derived parameters regarding early treatment response and the biological effect of RT. To become a clinically applicable approach, the IVIM/DKI technique must be standardized (measurement as well as signal modeling methods) and requires large-scale research studies.

### *OE-MRI*

In paper IV, six out of seven enrolled study patients had successfully acquired OE-MR data. One patient was excluded since the patient did not fit within the head coil with the breathing mask applied. The OE-MRI measurements were performed by acquisition of five dynamic MP2RAGE scans (i.e., dynamic TOLD series) with breathing of 100% O<sub>2</sub> during dynamic 2-4 (figure 5). T<sub>1</sub>-maps were derived from the dynamic TOLD series data using the Bloch equations for the MP2RAGE sequences and used for calculation of  $\Delta R_1$  within the tumor volume at both pre- and mid-RT. In addition, DCE data were used to classify voxels as perfused or non-perfused, and the perfused voxels were further classified as either perfused Oxy-E (normoxia) or perfused Oxy-R (hypoxia). Hence, for all study cases with available DCE data (three cases), all voxels within the GTV were classified as either perfused Oxy-E, perfused Oxy-R, or non-perfused (necrosis).

To ensure successful delivery of O<sub>2</sub> to the patients,  $\Delta R_1$  of the Oxy-E voxels in the dynamic TOLD series was monitored and expected to increase with O<sub>2</sub> inhalation (figure 5). This was indeed the case for all study patients and was also confirmed by an external pulse oximeter. However, independent quality control of oxygen delivery using the aorta<sup>121</sup> or nasal concha<sup>122</sup> might be valuable in the future. One drawback, however, of using the aorta or nasal concha as reference tissue could be the challenge of accurately delineating those small tissue volumes within the HN FOV. By dividing the tumor tissue into two subtypes; Oxy-E and Oxy-R, and analyzing the dynamic TOLD series of each subtype separately, an evaluation of the oxygen delivery was facilitated without the need for additional delineation.

The OE-MRI evaluation is dependent on the accuracy of the calculated T<sub>1</sub> map, and within Paper IV the T<sub>1</sub> maps were obtained via a lookup table generated with the Bloch equation for the MP2RAGE sequence<sup>123</sup>. As this T<sub>1</sub>-mapping technique is highly affected by the choice of sequence parameters, these were carefully selected to incorporate the transformation of signal to T<sub>1</sub>-values for both tumor and OARs<sup>124</sup>.

A decrease in the amount of tumor hypoxia, corresponding to an increased mean  $\Delta R_1$ , during the course of treatment is expected to be related to a positive RT treatment outcome. However, no relative change in population means  $\Delta R_1$  for pre- and mid-RT tumors were found for this study cohort in contrast to previously published data where an increase was reported for non-small cell lung cancer<sup>121</sup> and anal squamous cell carcinoma<sup>125</sup>. The individual evaluation showed an increase of the tumor mean  $\Delta R_1$  between initial and mid-treatment for two study cases, where one of those study cases also had IVIM parameters corresponding to a prediction of a positive treatment outcome (increase of  $D$  and  $f$ , decrease of  $K$ ). The remaining study cases had a decrease (three cases) or no change (one case) between the initial and treated tumor mean  $\Delta R_1$ . The sparsely reported OE-MRI-derived changes of RT highlight the need for further evaluation of the potential of this biomarker, and investigation of how to interpret the changes in relation to hypoxia during the course of RT.

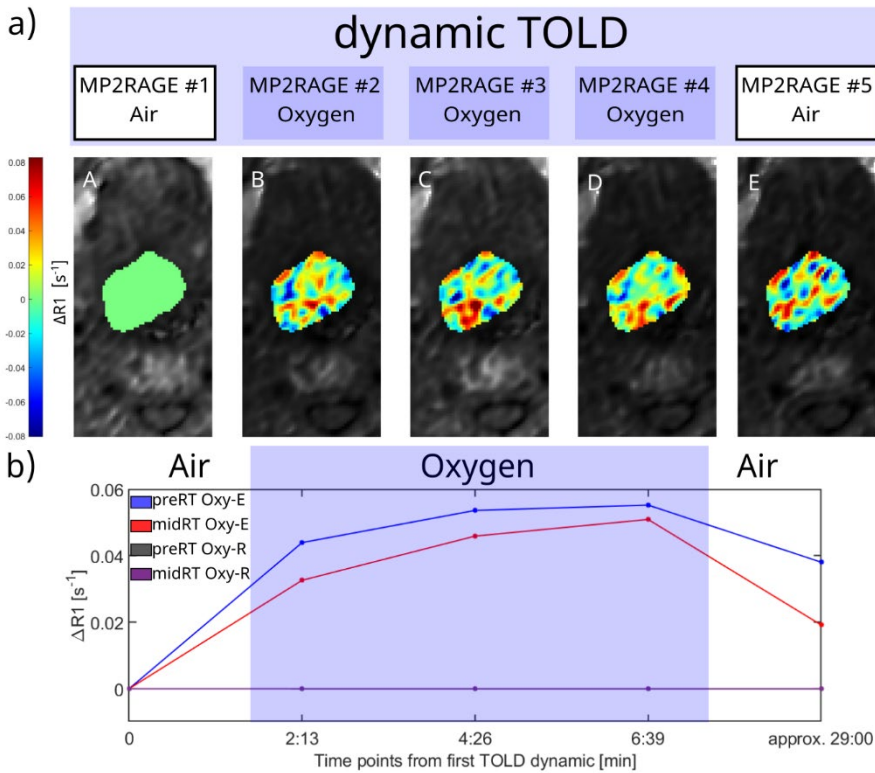


Figure 5. Illustration of Oxygen-Enhanced (OE) MRI for one study case. a) Five dynamic MP2RAGE images and the corresponding longitudinal  $\Delta R_1$  parameter maps (A-E) normalized towards MP2RAGE #1. The  $\Delta R_1$  parameter maps together with DCE data were used to classify perfused voxels as oxygen-enhancing (Oxy-E) or oxygen-refractory (Oxy-R). b) The mean  $\Delta R_1$  for Oxy-E classified voxels and Oxy-R

*classified voxels for each timepoint in the dynamic TOLD series, both before and during RT treatment. This study case shows successfully acquired OE-MRI data as Oxy-E classified voxels showed an increasing mean  $\Delta R_1$  while breathing 100% O<sub>2</sub>, not observed for Oxy-R classified voxels.*

## Challenges of multiparametric MRI in radiation therapy

Even though there are numerous multiparametric MRI techniques available for diagnostic purposes today, a direct translation from diagnostic MRI to a radiation therapy setting cannot be applied. For example, patient positioning during the MRI session for RT purposes is ideally acquired identical to the one at the treatment device. Although this was not the case for this study as the SNR in the DWI data became insufficient using the coil bridge support allowing for immobilization of the patient in RT position to be used for HN MRI. Instead, the standard head coil was used, leading to no treatment immobilization devices during the acquisition of the research pulse sequences.

Further, image distortion caused by the rapid image readout for some functional MRI techniques might be a challenge for proper implementation into radiation therapy. MRI-guided RT requires high geometric fidelity of the MRI data as violation of the spatial integrity of the anatomy within the MRI data might influence the precision of the treatment response assessment. The rather complex HN region has relatively high local susceptibility differences, leading to higher-order internal magnetic field inhomogeneities that influence the geometric accuracy of the MRI data, especially for single-shot EPI (ssEPI) which is used in most IVIM/DKI applications<sup>126</sup>. An alternative to ssEPI acquisition is diffusion-weighted turbo-spin-echo (DW-TSE), which uses multiple radio frequency refocusing pulses and, hence, is less prone to susceptibility effects but with a longer scan time compared to ssEPI<sup>127</sup>. Another alternative for DWI acquisition is multi-shot (segmented) EPI, which is less prone to susceptibility variations (i.e., reduced geometric distortions), and gives a possibility for improved spatial resolution, compared to ssEPI, although having a prolonged scan time. However, geometric correction of DWI images acquired with ssEPI could be conducted by calculation of field distortion maps<sup>82</sup> using the dual-echo T1-weighted Dixon data already acquired in the clinical MRI protocol for the HN study patients, hence the correction could be conducted without the need for additional imaging.

Another important aspect of MRI in RT is the limitation of examination time to minimize patient discomfort, especially when the imaging is performed in immobilized treatment positioning. During the OE-MRI, acquisition of two



baseline measurements would enable a voxel-wise statistical analysis of Oxy-E/R classification<sup>121</sup>, hence avoiding the population-based classification used in Paper IV but would come with the cost of extended imaging scan time. The use of multiple MP2RAGE sequences to acquire longitudinal  $T_1$  maps has the benefit of a large spatial coverage, often needed for RT purposes, but has a rather long total acquisition time. One way of shortening the total acquisition time is to use sequences that acquire more than two data points with different inversion times within one sequence scheme such as the modified Look-Locker inversion recovery (MOLLI) sequence or the saturation recovery single-shot acquisition (SASHA) sequence<sup>128</sup>. These types of sequences are often used for 2D mapping within cardiovascular MRI where there is a considerably smaller need for large spatial coverage.



## Conclusions

This thesis includes validation of synthetic CT data (sCT) usage in a number of individual steps of the radiation therapy (RT) process, all significantly contributing to increased feasibility of clinical implementation of MRI-only based RT for several different cancer types. In addition, the thesis addresses the possibility of implementing multiparametric MRI for tumor characterization and treatment follow-up in the RT process for the rather complex head and neck (HN) region.

Specifically, it was shown that

- a deep-learning generated sCT has comparable geometric and dosimetric performance as genuine CT data and hence can be used in HN cancer treatment planning (Paper I)
- the deep-learning generated sCT has comparable 2D and 3D patient positioning registrations as the original CT data and hence can be used for HN treatment positioning (Paper II)
- recalculated dose distribution using cone beam CT data from prostate cancer patients provides comparable dosimetric results as the calculated sCT-based dose distribution and can be used as a feasible quality assurance tool to detect gross generation errors within the sCT data (Paper III)
- it is clinically feasible to implement Oxygen-Enhanced (OE) MRI, intravoxel incoherent motion (IVIM), and diffusion kurtosis imaging (DKI) within MRI in RT for HN cancers and these methods are promising tools for early response assessment (Paper IV).



## Future perspectives

The use of MRI in RT is increasing and recently hybrid MRI-linear accelerators have been presented, combining a linear accelerator with an MRI simulator. This provides MRI-guided radiation therapy (MRgRT) with real-time MR imaging and subsequently real-time tracking of soft tissue for intrafraction motions adaptation as well as adaptation of the treatment plan on a day-to-day basis<sup>129,130</sup>. Clinical translation from the traditional workflow to MRI-only workflow is ongoing, and few clinics worldwide have implemented an MRI-only workflow without any additional imaging modalities required<sup>42</sup>. The clinics that do have a genuine MRI-only workflow implemented have reported results from treatment of prostate and brain. Additional clinics have MRI-only workflows implemented for prostate<sup>42</sup> and brain<sup>39</sup> but still acquired CT for QA purposes. Approximately half of the reported studies utilized a commercial sCT generation method, simplifying the standardization of the MRI-only workflow. As the current implementations and sCT generation methods mainly have been focused on prostate and brain, it is essential to perform validations for other treatment sites in order to move towards a broader implementation of MRI-only workflows. As the HN area is a complex region and hence has difficulties with reproducible repositioning and co-registering between different imaging modalities<sup>131</sup>, it might highly benefit from transition to an MRI-only workflow, reducing the multimodal imaging registration uncertainties. However, further studies are required to fully establish the potential gain. As MRI is the only modality available once CT is excluded from the treatment workflow, it is essential to evaluate potential changes in delineation of target and OARs. For example, a decreased delineation volume of the prostate has been reported for an MRI-only workflow compared to the traditional MRI and CT-based workflow<sup>132</sup>. A reduced treatment volume as an outcome of an MRI-only prostate workflow provides potential to deliver less radiation to adjacent OARs and hence fewer side effects for this patient group. However, whether such observed changes in delineation will be observed for other anatomical regions requires further studies.

The development of multiparametric MRI to assess and characterize physiological heterogeneity within the tumor and OARs could be a key factor for development of new radiation therapy approaches targeting heterogeneity and improving treatment outcomes. By visualization of hypoxic regions within the tumor through parameter maps (e.g., perfused Oxy-R classified voxels, low D and f, and high K), RT planning of localized treatment intensification or de-escalation strategies could be applied and thereby enable an adaptive and individualized RT-treatment. A voxel-based evaluation of the correlation

between IVIM parameters and OE-MRI parameters would be of interest. However, this requires MRI data with high geometric accuracy and spatial resolution, which today is limited by the current system performance. In addition, before implementing individualized RT, the biological reflection of each biomarker must be determined, which requires substantial evaluations with standardized multiparametric MRI methods, preferably worldwide. It has been shown that  $f$  and tumor blood flow correlates for HN cancer where segmented fitting had a better correlation than direct fitting<sup>133</sup>, although contraindications for other tumor sites exist<sup>134</sup>. Further evaluation of the correlation between  $f$  and DCE is of major interest as it could enable non-invasive IVIM data to be used to classify hypoxic areas within the OE-MRI data, hence avoiding the need for Gd-CA administration to the patient.

# Acknowledgment

I would like to express my gratitude to all the people who in many ways have supported and helped me during this education. It would not be feasible to complete this thesis without you.

I am so grateful to my main supervisor Maja Sohlén, for taking a chance on me as your first PhD student. I will always appreciate the opportunity you brought to work with MR in radiation therapy. Also, thank you for your patience, continuous support, and the invaluable contributions you have made in our many discussions.

I would also like to thank my co-supervisors, Anna Karlsson, Fredrik Nordström, and Karin Petruson, for your knowledge that has made an important impact on my work. A special thanks to Maria Ljungberg, for your advice and expertise, and for constantly being available to hear me out.

Thanks to the staff at the radiation department, especially Mariana and Mitra, for sharing your skills and the endless fun conversations. Without your support, there would not be any data for me to evaluate.

My roommates Frida, Louise, Jens, Lukas, and Mikael, thank you for the great company and the nicest coffee breaks. You are the reason our office is as enjoyable as it can be. I would also like to thank my colleagues in the MR physics group, Kerstin, Jesper, Oscar, Nicolas, Linnéa, Evin, Stefanie, Stefan, Göran, Jonathan, Christian, Lars, and Frida, for making it such a welcoming and pleasant place to work at. No doubt you bring joy to the lunches.

To my fellow PhD students and the permanent staff at the department of medical radiation sciences, thank you for all the good times, both in and out of office.

Till mina fantastiska vänner och underbara familj, jag kan inte tacka nog för alla aktiviteter, konversationer och öl som har inmundigats de senaste åren. Allt är ljusare och lättare med er i min vardag.





## References

1. Sung H, Ferlay J, Siegel RL, et al. Global Cancer Statistics 2020: GLOBOCAN Estimates of Incidence and Mortality Worldwide for 36 Cancers in 185 Countries. *CA: A Cancer Journal for Clinicians*. 2021;71(3):209-249.
2. Dawson LA, Ménard C. Imaging in radiation oncology: a perspective [published online ahead of print 2010/04/24]. *Oncologist*. 2010;15(4):338-349.
3. Khoo VS, Joon DL. New developments in MRI for target volume delineation in radiotherapy [published online ahead of print 2006/09/19]. *Br J Radiol*. 2006;79 Spec No 1:S2-15.
4. Das IJ, McGee KP, Tyagi N, Wang H. Role and future of MRI in radiation oncology [published online ahead of print 2018/11/02]. *Br J Radiol*. 2019;92(1094):20180505.
5. Jonsson J, Nyholm T, Söderkvist K. The rationale for MR-only treatment planning for external radiotherapy [published online ahead of print 2019/07/26]. *Clin Transl Radiat Oncol*. 2019;18:60-65.
6. Edmund JM, Nyholm T. A review of substitute CT generation for MRI-only radiation therapy [published online ahead of print 2017/01/28]. *Radiat Oncol*. 2017;12(1):28.
7. Johnstone E, Wyatt JJ, Henry AM, et al. Systematic Review of Synthetic Computed Tomography Generation Methodologies for Use in Magnetic Resonance Imaging-Only Radiation Therapy [published online ahead of print 2017/12/20]. *Int J Radiat Oncol Biol Phys*. 2018;100(1):199-217.
8. Owraangi AM, Greer PB, Glide-Hurst CK. MRI-only treatment planning: benefits and challenges [published online ahead of print 2018/02/03]. *Phys Med Biol*. 2018;63(5):05tr01.
9. Gurney-Champion OJ, Mahmood F, van Schie M, et al. Quantitative imaging for radiotherapy purposes [published online ahead of print 2020/03/03]. *Radiother Oncol*. 2020;146:66-75.
10. Martens RM, Koopman T, Lavini C, et al. Early Response Prediction of Multiparametric Functional MRI and (18)F-FDG-PET in Patients with Head and Neck Squamous Cell Carcinoma Treated with (Chemo)Radiation [published online ahead of print 2022/01/12]. *Cancers (Basel)*. 2022;14(1).
11. Tatum JL, Kelloff GJ, Gillies RJ, et al. Hypoxia: importance in tumor biology, noninvasive measurement by imaging, and value of its measurement in the management of cancer therapy [published online ahead of print 2006/11/23]. *Int J Radiat Biol*. 2006;82(10):699-757.
12. O'Connor JPB, Robinson SP, Waterton JC. Imaging tumour hypoxia with oxygen-enhanced MRI and BOLD MRI [published online ahead of print 2018/10/03]. *Br J Radiol*. 2019;92(1095):20180642.

13. *Transition from 2-D Radiotherapy to 3-D Conformal and Intensity Modulated Radiotherapy*. Vienna: INTERNATIONAL ATOMIC ENERGY AGENCY; 2008.
14. Njeh CF. Tumor delineation: The weakest link in the search for accuracy in radiotherapy [published online ahead of print 2009/11/07]. *J Med Phys*. 2008;33(4):136-140.
15. Ten Haken RK, Thornton AF, Jr., Sandler HM, et al. A quantitative assessment of the addition of MRI to CT-based, 3-D treatment planning of brain tumors [published online ahead of print 1992/10/11]. *Radiother Oncol*. 1992;25(2):121-133.
16. Khoo VS, Adams EJ, Saran F, et al. A Comparison of clinical target volumes determined by CT and MRI for the radiotherapy planning of base of skull meningiomas [published online ahead of print 2000/03/22]. *Int J Radiat Oncol Biol Phys*. 2000;46(5):1309-1317.
17. Hentschel B, Oehler W, Strauss D, Ulrich A, Malich A. Definition of the CTV prostate in CT and MRI by using CT-MRI image fusion in IMRT planning for prostate cancer [published online ahead of print 2011/02/25]. *Strahlenther Onkol*. 2011;187(3):183-190.
18. Roach M, 3rd, Faillace-Akazawa P, Malfatti C, Holland J, Hricak H. Prostate volumes defined by magnetic resonance imaging and computerized tomographic scans for three-dimensional conformal radiotherapy [published online ahead of print 1996/07/15]. *Int J Radiat Oncol Biol Phys*. 1996;35(5):1011-1018.
19. Rasch C, Steenbakkers R, van Herk M. Target definition in prostate, head, and neck [published online ahead of print 2005/06/29]. *Semin Radiat Oncol*. 2005;15(3):136-145.
20. Coen R, Ronald K, Frank AP, et al. The potential impact of CT-MRI matching on tumor volume delineation in advanced head and neck cancer. *International Journal of Radiation Oncology Biology Physics*. 1997;39:841-848.
21. Thiagarajan A, Caria N, Schöder H, et al. Target volume delineation in oropharyngeal cancer: impact of PET, MRI, and physical examination [published online ahead of print 2011/11/01]. *Int J Radiat Oncol Biol Phys*. 2012;83(1):220-227.
22. Aoyama H, Shirato H, Nishioka T, et al. Magnetic resonance imaging system for three-dimensional conformal radiotherapy and its impact on gross tumor volume delineation of central nervous system tumors [published online ahead of print 2001/06/08]. *Int J Radiat Oncol Biol Phys*. 2001;50(3):821-827.
23. Wachter S, Wachter-Gerstner N, Bock T, et al. Interobserver comparison of CT and MRI-based prostate apex definition. Clinical relevance for conformal radiotherapy treatment planning [published online ahead of print 2002/06/27]. *Strahlenther Onkol*. 2002;178(5):263-268.

24. Rasch C, Keus R, Pameijer FA, et al. The potential impact of CT-MRI matching on tumor volume delineation in advanced head and neck cancer [published online ahead of print 1997/11/22]. *Int J Radiat Oncol Biol Phys*. 1997;39(4):841-848.
25. Hoskin PJ. Hypoxia dose painting in prostate and cervix cancer. *Acta Oncologica*. 2015;54(9):1259-1262.
26. van der Heide UA, Houweling AC, Groenendaal G, Beets-Tan RG, Lambin P. Functional MRI for radiotherapy dose painting [published online ahead of print 2012/07/10]. *Magn Reson Imaging*. 2012;30(9):1216-1223.
27. Walker A, Liney G, Metcalfe P, Holloway L. MRI distortion: considerations for MRI based radiotherapy treatment planning [published online ahead of print 2014/02/13]. *Australas Phys Eng Sci Med*. 2014;37(1):103-113.
28. Weygand J, Fuller CD, Ibbott GS, et al. Spatial Precision in Magnetic Resonance Imaging-Guided Radiation Therapy: The Role of Geometric Distortion [published online ahead of print 2016/06/30]. *Int J Radiat Oncol Biol Phys*. 2016;95(4):1304-1316.
29. Daisne JF, Sibomana M, Bol A, Cosnard G, Lonnet M, Grégoire V. Evaluation of a multimodality image (CT, MRI and PET) coregistration procedure on phantom and head and neck cancer patients: accuracy, reproducibility and consistency [published online ahead of print 2003/12/04]. *Radiother Oncol*. 2003;69(3):237-245.
30. Ulin K, Urie MM, Cherlow JM. Results of a multi-institutional benchmark test for cranial CT/MR image registration [published online ahead of print 2010/04/13]. *Int J Radiat Oncol Biol Phys*. 2010;77(5):1584-1589.
31. Persson E, Emin S, Scherman J, et al. Investigation of the clinical inter-observer bias in prostate fiducial marker image registration between CT and MR images. *Radiation Oncology*. 2021;16(1):150.
32. Roberson PL, McLaughlin PW, Narayana V, Troyer S, Hixson GV, Kessler ML. Use and uncertainties of mutual information for computed tomography/ magnetic resonance (CT/MR) registration post permanent implant of the prostate [published online ahead of print 2005/03/26]. *Med Phys*. 2005;32(2):473-482.
33. Mutic S, Dempsey JF, Bosch WR, et al. Multimodality image registration quality assurance for conformal three-dimensional treatment planning [published online ahead of print 2001/08/23]. *Int J Radiat Oncol Biol Phys*. 2001;51(1):255-260.
34. Seppälä T, Visapää H, Collan J, et al. Converting from CT- to MRI-only-based target definition in radiotherapy of localized prostate cancer: A comparison between two modalities [published online ahead of print 2015/07/15]. *Strahlenther Onkol*. 2015;191(11):862-868.
35. Christiansen RL, Jensen HR, Brink C. Magnetic resonance only workflow and validation of dose calculations for radiotherapy of

- prostate cancer [published online ahead of print 2017/05/04]. *Acta Oncol.* 2017;56(6):787-791.
36. Tenhunen M, Korhonen J, Kapanen M, et al. MRI-only based radiation therapy of prostate cancer: workflow and early clinical experience [published online ahead of print 2018/03/01]. *Acta Oncol.* 2018;57(7):902-907.
37. Persson E, Jamtheim Gustafsson C, Ambolt P, et al. MR-PROTECT: Clinical feasibility of a prostate MRI-only radiotherapy treatment workflow and investigation of acceptance criteria. *Radiation Oncology.* 2020;15(1):77.
38. Greer P, Martin J, Sidhom M, et al. A Multi-center Prospective Study for Implementation of an MRI-Only Prostate Treatment Planning Workflow [published online ahead of print 2019/09/27]. *Front Oncol.* 2019;9:826.
39. Lerner M, Medin J, Jamtheim Gustafsson C, Alkner S, Olsson LE. Prospective Clinical Feasibility Study for MRI-Only Brain Radiotherapy [published online ahead of print 2022/01/28]. *Front Oncol.* 2021;11:812643.
40. Boulanger M, Nunes JC, Chourak H, et al. Deep learning methods to generate synthetic CT from MRI in radiotherapy: A literature review [published online ahead of print 2021/09/03]. *Phys Med.* 2021;89:265-281.
41. Tyagi N. Challenges and Requirements. In: Liney G, van der Heide U, eds. *MRI for Radiotherapy: Planning, Delivery, and Response Assessment*. doi: 10.1007/978-3-030-14442-5\_8 Cham: Springer International Publishing; 2019:119-129.
42. Dowling JA, Korhonen J. MR-Only Methodology. *MRI for Radiotherapy.* 2019.
43. Dowling J, O'Connor L, Acosta O, et al. Chapter 20 - Image synthesis for MRI-only radiotherapy treatment planning. In: Burgos N, Svoboda D, eds. *Biomedical Image Synthesis and Simulation*. doi: <https://doi.org/10.1016/B978-0-12-824349-7.00027-X>: Academic Press; 2022:423-445.
44. Siversson C, Nordström F, Nilsson T, et al. Technical Note: MRI only prostate radiotherapy planning using the statistical decomposition algorithm. *Medical Physics.* 2015;42(10):6090-6097.
45. Spadea MF, Maspero M, Zaffino P, Seco J. Deep learning based synthetic-CT generation in radiotherapy and PET: A review. *Medical Physics.* 2021;48(11):6537-6566.
46. Wang T, Lei Y, Fu Y, et al. A review on medical imaging synthesis using deep learning and its clinical applications. *Journal of Applied Clinical Medical Physics.* 2021;22(1):11-36.
47. Cronholm R, Karlsson A, Siversson C. MRI only radiotherapy planning using the transfer function estimation algorithm2020, [http://www.spectronic.se/files/Whitepaper\\_TFE\\_202106.pdf](http://www.spectronic.se/files/Whitepaper_TFE_202106.pdf).

48. Tyagi N, Fontenla S, Zhang J, et al. Dosimetric and workflow evaluation of first commercial synthetic CT software for clinical use in pelvis [published online ahead of print 2016/12/17]. *Phys Med Biol*. 2017;62(8):2961-2975.
49. Köhler M, Vaara T, Van Grootel M, Hoogeveen R, Kemppainen R, Renisch S. *MR-only simulation for radiotherapy planning treatment planning*  
[https://www.documents.philips.com/doclib/enc/fetch/2000/4504/577242/577251/587787/White\\_Paper\\_MR-only\\_sim\\_LR.pdf](https://www.documents.philips.com/doclib/enc/fetch/2000/4504/577242/577251/587787/White_Paper_MR-only_sim_LR.pdf)2015.
50. Gonzalez-Moya A, Dufreneix S, Ouyessad N, Guillerminet C, Autret D. Evaluation of a commercial synthetic computed tomography generation solution for magnetic resonance imaging-only radiotherapy [published online ahead of print 2021/05/28]. *J Appl Clin Med Phys*. 2021;22(6):191-197.
51. GmbH SH. *White paper MR-only RT planning for the brain and pelvis with Synthetic CT*.  
[https://cdn0.scrvt.com/39b415fb07de4d9656c7b516d8e2d907/180000006768945/1ed4126c4f76/Whitepaper-MR-only-RT-planning-for-the-brain-and-pelvis-with-synthetic.CT\\_180000006768945.pdf](https://cdn0.scrvt.com/39b415fb07de4d9656c7b516d8e2d907/180000006768945/1ed4126c4f76/Whitepaper-MR-only-RT-planning-for-the-brain-and-pelvis-with-synthetic.CT_180000006768945.pdf)2019.
52. Persson E, Gustafsson C, Nordström F, et al. MR-OPERA: A Multicenter/Multivendor Validation of Magnetic Resonance Imaging-Only Prostate Treatment Planning Using Synthetic Computed Tomography Images [published online ahead of print 2017/08/28]. *Int J Radiat Oncol Biol Phys*. 2017;99(3):692-700.
53. Hoesl M, Escobar Corral N, Mistry N. *White paper MR-based Synthetic CT reimaged* <https://marketing.webassets.siemens-healthineers.com/14a780979ccdde45/657cf9efc589/White-Paper-MR-based-Synthetic-CT.PDF>2022.
54. Jens ME, Hans MK, Koen Van L, Rasmus HH, Jon ALA, Daniel A. A voxel-based investigation for MRI-only radiotherapy of the brain using ultra short echo times. *Physics in Medicine and Biology*. 2014;59:7501-7519.
55. Palmér E, Karlsson A, Nordström F, et al. Synthetic computed tomography data allows for accurate absorbed dose calculations in a magnetic resonance imaging only workflow for head and neck radiotherapy [published online ahead of print 2021/04/27]. *Phys Imaging Radiat Oncol*. 2021;17:36-42.
56. Dinkla AM, Florkow MC, Maspero M, et al. Dosimetric evaluation of synthetic CT for head and neck radiotherapy generated by a patch-based three-dimensional convolutional neural network [published online ahead of print 2019/06/18]. *Med Phys*. 2019;46(9):4095-4104.
57. Klages P, Benslimane I, Riyahi S, et al. Patch-based generative adversarial neural network models for head and neck MR-only

- planning [published online ahead of print 2019/11/17]. *Med Phys.* 2020;47(2):626-642.
58. Peng Y, Chen S, Qin A, et al. Magnetic resonance-based synthetic computed tomography images generated using generative adversarial networks for nasopharyngeal carcinoma radiotherapy treatment planning. *Radiotherapy and Oncology.* 2020;150:217-224.
59. Qi M, Li Y, Wu A, et al. Multi-sequence MR image-based synthetic CT generation using a generative adversarial network for head and neck MRI-only radiotherapy [published online ahead of print 2020/02/07]. *Med Phys.* 2020;47(4):1880-1894.
60. Huttenlocher DP, Klanderman GA, Rucklidge WJ. Comparing images using the Hausdorff distance. *IEEE Transactions on Pattern Analysis and Machine Intelligence.* 1993;15(9):850-863.
61. Wang Y, Liu C, Zhang X, Deng W. Synthetic CT Generation Based on T2 Weighted MRI of Nasopharyngeal Carcinoma (NPC) Using a Deep Convolutional Neural Network (DCNN) [published online ahead of print 2019/12/19]. *Front Oncol.* 2019;9:1333.
62. Largent A, Marage L, Gicquiau I, et al. Head-and-Neck MRI-only radiotherapy treatment planning: From acquisition in treatment position to pseudo-CT generation [published online ahead of print 2020/03/18]. *Cancer Radiother.* 2020;24(4):288-297.
63. Tie X, Lam SK, Zhang Y, Lee KH, Au KH, Cai J. Pseudo-CT generation from multi-parametric MRI using a novel multi-channel multi-path conditional generative adversarial network for nasopharyngeal carcinoma patients [published online ahead of print 2020/02/06]. *Med Phys.* 2020;47(4):1750-1762.
64. Price RG, Kim JP, Zheng W, Chetty IJ, Glide-Hurst C. Image Guided Radiation Therapy Using Synthetic Computed Tomography Images in Brain Cancer [published online ahead of print 2016/05/23]. *Int J Radiat Oncol Biol Phys.* 2016;95(4):1281-1289.
65. Korhonen J, Kapanen M, Sonke JJ, et al. Feasibility of MRI-based reference images for image-guided radiotherapy of the pelvis with either cone-beam computed tomography or planar localization images [published online ahead of print 2014/09/19]. *Acta Oncol.* 2015;54(6):889-895.
66. Maspero M, Tyyger MD, Tijssen RHN, Seevinck PR, Intven MPW, van den Berg CAT. Feasibility of magnetic resonance imaging-only rectum radiotherapy with a commercial synthetic computed tomography generation solution. *Physics and imaging in radiation oncology.* 2018;7:58-64.
67. Kempainen R, Suilamo S, Ranta I, et al. Assessment of dosimetric and positioning accuracy of a magnetic resonance imaging-only solution for external beam radiotherapy of pelvic anatomy [published online ahead of print 2019/06/22]. *Phys Imaging Radiat Oncol.* 2019;11:1-8.

68. Edmund JM, Andreasen D, Mahmood F, Van Leemput K. Cone beam computed tomography guided treatment delivery and planning verification for magnetic resonance imaging only radiotherapy of the brain [published online ahead of print 2015/07/23]. *Acta Oncol.* 2015;54(9):1496-1500.
69. Edmund JM, Andreasen D, Van Leemput K. Cone beam computed tomography based image guidance and quality assessment of prostate cancer for magnetic resonance imaging-only radiotherapy in the pelvis. *Physics and Imaging in Radiation Oncology.* 2021;18:55-60.
70. Gupta D, Kim M, Vineberg KA, Balter JM. Generation of Synthetic CT Images From MRI for Treatment Planning and Patient Positioning Using a 3-Channel U-Net Trained on Sagittal Images [published online ahead of print 2019/10/15]. *Front Oncol.* 2019;9:964.
71. Lerner M, Medin J, Jamtheim Gustafsson C, Alkner S, Siversson C, Olsson LE. Clinical validation of a commercially available deep learning software for synthetic CT generation for brain [published online ahead of print 2021/04/09]. *Radiat Oncol.* 2021;16(1):66.
72. Palmér E, Nordström F, Karlsson A, Petruson K, Ljungberg M, Sohlín M. Head and neck cancer patient positioning using synthetic CT data in MRI-only radiation therapy [published online ahead of print 2022/01/20]. *J Appl Clin Med Phys.* 2022;23(4):e13525.
73. Vandewinckele L, Claessens M, Dinkla A, et al. Overview of artificial intelligence-based applications in radiotherapy: Recommendations for implementation and quality assurance [published online ahead of print 2020/09/14]. *Radiother Oncol.* 2020;153:55-66.
74. Choi JH, Lee D, O'Connor L, et al. Bulk Anatomical Density Based Dose Calculation for Patient-Specific Quality Assurance of MRI-Only Prostate Radiotherapy [published online ahead of print 2019/10/22]. *Front Oncol.* 2019;9:997.
75. Palmér E, Persson E, Ambolt P, Gustafsson C, Gunnlaugsson A, Olsson LE. Cone beam CT for QA of synthetic CT in MRI only for prostate patients [published online ahead of print 2018/09/06]. *J Appl Clin Med Phys.* 2018;19(6):44-52.
76. Palmér E, Sohlín M, Petruson K, Ljungberg M, Karlsson A. [P269] Absorbed dose calculation based on CBCT data for head and neck cancer patients. *Physica Medica.* 2018;52:177.
77. Irmak S, Zimmermann L, Georg D, Kuess P, Lechner W. Cone beam CT based validation of neural network generated synthetic CTs for radiotherapy in the head region. *Medical Physics.* 2021;48(8):4560-4571.
78. Adjeiwaah M, Bylund M, Lundman JA, et al. Dosimetric Impact of MRI Distortions: A Study on Head and Neck Cancers [published online ahead of print 2018/11/30]. *Int J Radiat Oncol Biol Phys.* 2019;103(4):994-1003.

79. Adjeiwaah M, Bylund M, Lundman JA, Karlsson CT, Jonsson JH, Nyholm T. Quantifying the Effect of 3T Magnetic Resonance Imaging Residual System Distortions and Patient-Induced Susceptibility Distortions on Radiation Therapy Treatment Planning for Prostate Cancer [published online ahead of print 2017/12/13]. *Int J Radiat Oncol Biol Phys*. 2018;100(2):317-324.
80. Gustafsson C, Nordström F, Persson E, Brynolfsson J, Olsson LE. Assessment of dosimetric impact of system specific geometric distortion in an MRI only based radiotherapy workflow for prostate. *Physics in Medicine and Biology*. 2017;62:2976-2989.
81. Browall J, Palmér E, Sohlin M, Ljungberg M. *Dosimetric impact of system specific geometric distortion on head and neck treatment plans in MRI only based radiation therapy.* [https://radfys.gu.se/digitalAssets/1736/1736501\\_jesper-browall-examensarbete.pdf](https://radfys.gu.se/digitalAssets/1736/1736501_jesper-browall-examensarbete.pdf)2019.
82. Jezzard P, Balaban RS. Correction for geometric distortion in echo planar images from B0 field variations [published online ahead of print 1995/07/01]. *Magn Reson Med*. 1995;34(1):65-73.
83. Press RH, Shu HG, Shim H, et al. The Use of Quantitative Imaging in Radiation Oncology: A Quantitative Imaging Network (QIN) Perspective [published online ahead of print 2018/07/04]. *Int J Radiat Oncol Biol Phys*. 2018;102(4):1219-1235.
84. Hill RP, Bristow RG, Fyles A, Koritzinsky M, Milosevic M, Wouters BG. Hypoxia and Predicting Radiation Response [published online ahead of print 2015/09/19]. *Semin Radiat Oncol*. 2015;25(4):260-272.
85. Höckel M, Vaupel P. Tumor Hypoxia: Definitions and Current Clinical, Biologic, and Molecular Aspects. *JNCI: Journal of the National Cancer Institute*. 2001;93(4):266-276.
86. Hall EJ, Giaccia AJ. *Radiobiology for the radiologist: Seventh edition*. 2012.
87. Nordsmark M, Bentzen SM, Rudat V, et al. Prognostic value of tumor oxygenation in 397 head and neck tumors after primary radiation therapy. An international multi-center study. *Radiotherapy and Oncology*. 2005;77(1):18-24.
88. Paterson C, Hargreaves S, Rumley CN. Functional Imaging to Predict Treatment Response in Head and Neck Cancer: How Close are We to Biologically Adaptive Radiotherapy? [published online ahead of print 2020/11/01]. *Clin Oncol (R Coll Radiol)*. 2020;32(12):861-873.
89. Wiedenmann NE, Bucher S, Hentschel M, et al. Serial [18F]-fluoromisonidazole PET during radiochemotherapy for locally advanced head and neck cancer and its correlation with outcome [published online ahead of print 2015/10/04]. *Radiother Oncol*. 2015;117(1):113-117.
90. Zips D, Zöphel K, Abolmaali N, et al. Exploratory prospective trial of hypoxia-specific PET imaging during radiochemotherapy in patients



- with locally advanced head-and-neck cancer [published online ahead of print 2012/10/02]. *Radiother Oncol.* 2012;105(1):21-28.
91. Löck S, Perrin R, Seidlitz A, et al. Residual tumour hypoxia in head-and-neck cancer patients undergoing primary radiochemotherapy, final results of a prospective trial on repeat FMISO-PET imaging [published online ahead of print 2017/08/28]. *Radiother Oncol.* 2017;124(3):533-540.
92. Jahng GH, Li KL, Ostergaard L, Calamante F. Perfusion magnetic resonance imaging: a comprehensive update on principles and techniques [published online ahead of print 2014/09/24]. *Korean J Radiol.* 2014;15(5):554-577.
93. Connolly M, Srinivasan A. Diffusion-Weighted Imaging in Head and Neck Cancer: Technique, Limitations, and Applications [published online ahead of print 2017/11/13]. *Magn Reson Imaging Clin N Am.* 2018;26(1):121-133.
94. Baboli M, Zhang J, Kim SG. Advances in Diffusion and Perfusion MRI for Quantitative Cancer Imaging [published online ahead of print 2020/12/22]. *Curr Pathobiol Rep.* 2019;7(4):129-141.
95. Thoeny HC, De Keyser F, King AD. Diffusion-weighted MR imaging in the head and neck [published online ahead of print 2012/03/23]. *Radiology.* 2012;263(1):19-32.
96. Wang J, Takashima S, Takayama F, et al. Head and neck lesions: characterization with diffusion-weighted echo-planar MR imaging [published online ahead of print 2001/08/30]. *Radiology.* 2001;220(3):621-630.
97. Srinivasan A, Dvorak R, Perni K, Rohrer S, Mukherji SK. Differentiation of benign and malignant pathology in the head and neck using 3T apparent diffusion coefficient values: early experience [published online ahead of print 2007/10/09]. *AJNR Am J Neuroradiol.* 2008;29(1):40-44.
98. Razek AA, Elkhamary S, Mousa A. Differentiation between benign and malignant orbital tumors at 3-T diffusion MR-imaging [published online ahead of print 2011/02/03]. *Neuroradiology.* 2011;53(7):517-522.
99. Le Bihan D, Breton E, Lallemand D, Aubin ML, Vignaud J, Laval-Jeantet M. Separation of diffusion and perfusion in intravoxel incoherent motion MR imaging [published online ahead of print 1988/08/01]. *Radiology.* 1988;168(2):497-505.
100. Le Bihan D, Breton E, Lallemand D, Grenier P, Cabanis E, Laval-Jeantet M. MR imaging of intravoxel incoherent motions: application to diffusion and perfusion in neurologic disorders [published online ahead of print 1986/11/01]. *Radiology.* 1986;161(2):401-407.
101. Le Bihan D. What can we see with IVIM MRI? *NeuroImage.* 2019;187:56-67.

102. Merisaari H, Movahedi P, Perez IM, et al. Fitting methods for intravoxel incoherent motion imaging of prostate cancer on region of interest level: Repeatability and gleason score prediction [published online ahead of print 2016/03/01]. *Magn Reson Med*. 2017;77(3):1249-1264.
103. Jalnefjord O, Andersson M, Montelius M, et al. Comparison of methods for estimation of the intravoxel incoherent motion (IVIM) diffusion coefficient (D) and perfusion fraction (f). *Magnetic Resonance Materials in Physics, Biology and Medicine*. 2018;31(6):715-723.
104. Jensen JH, Helpert JA, Ramani A, Lu H, Kaczynski K. Diffusional kurtosis imaging: the quantification of non-gaussian water diffusion by means of magnetic resonance imaging [published online ahead of print 2005/05/21]. *Magn Reson Med*. 2005;53(6):1432-1440.
105. Iima M, Le Bihan D. Clinical Intravoxel Incoherent Motion and Diffusion MR Imaging: Past, Present, and Future [published online ahead of print 2015/12/23]. *Radiology*. 2016;278(1):13-32.
106. O'Connor JP, Boulton JK, Jamin Y, et al. Oxygen-Enhanced MRI Accurately Identifies, Quantifies, and Maps Tumor Hypoxia in Preclinical Cancer Models [published online ahead of print 2015/12/15]. *Cancer Res*. 2016;76(4):787-795.
107. Therasse P, Arbuck SG, Eisenhauer EA, et al. New guidelines to evaluate the response to treatment in solid tumors. European Organization for Research and Treatment of Cancer, National Cancer Institute of the United States, National Cancer Institute of Canada [published online ahead of print 2000/02/03]. *J Natl Cancer Inst*. 2000;92(3):205-216.
108. Hatakenaka M, Nakamura K, Yabuuchi H, et al. Apparent diffusion coefficient is a prognostic factor of head and neck squamous cell carcinoma treated with radiotherapy [published online ahead of print 2014/01/11]. *Jpn J Radiol*. 2014;32(2):80-89.
109. Srinivasan A, Chenevert TL, Dwamena BA, et al. Utility of pretreatment mean apparent diffusion coefficient and apparent diffusion coefficient histograms in prediction of outcome to chemoradiation in head and neck squamous cell carcinoma [published online ahead of print 2012/01/21]. *J Comput Assist Tomogr*. 2012;36(1):131-137.
110. Kim S, Loevner L, Quon H, et al. Diffusion-weighted magnetic resonance imaging for predicting and detecting early response to chemoradiation therapy of squamous cell carcinomas of the head and neck [published online ahead of print 2009/02/04]. *Clin Cancer Res*. 2009;15(3):986-994.
111. Jalnefjord O, Montelius M, Starck G, Ljungberg M. Optimization of b-value schemes for estimation of the diffusion coefficient and the perfusion fraction with segmented intravoxel incoherent motion model

- fitting [published online ahead of print 2019/05/31]. *Magn Reson Med*. 2019;82(4):1541-1552.
112. Fujima N, Yoshida D, Sakashita T, et al. Prediction of the treatment outcome using intravoxel incoherent motion and diffusional kurtosis imaging in nasal or sinonasal squamous cell carcinoma patients [published online ahead of print 2016/06/04]. *Eur Radiol*. 2017;27(3):956-965.
  113. Fujima N, Sakashita T, Homma A, Yoshida D, Kudo K, Shirato H. Utility of a Hybrid IVIM-DKI Model to Predict the Development of Distant Metastasis in Head and Neck Squamous Cell Carcinoma Patients [published online ahead of print 2017/05/19]. *Magn Reson Med Sci*. 2018;17(1):21-27.
  114. Hejduk B, Bobek-Billewicz B, Rutkowski T, Hebda A, Zawadzka A, Jurkowski MK. Application of Intravoxel Incoherent Motion (IVIM) Model for Differentiation Between Metastatic and Non-Metastatic Head and Neck Lymph Nodes [published online ahead of print 2018/04/18]. *Pol J Radiol*. 2017;82:506-510.
  115. Hauser T, Essig M, Jensen A, et al. Prediction of treatment response in head and neck carcinomas using IVIM-DWI: Evaluation of lymph node metastasis [published online ahead of print 2014/03/19]. *Eur J Radiol*. 2014;83(5):783-787.
  116. Marzi S, Farneti A, Vidiri A, et al. Radiation-induced parotid changes in oropharyngeal cancer patients: the role of early functional imaging and patient-/treatment-related factors. *Radiation Oncology*. 2018;13(1):189.
  117. Marzi S, Forina C, Marucci L, et al. Early radiation-induced changes evaluated by intravoxel incoherent motion in the major salivary glands [published online ahead of print 2014/04/05]. *J Magn Reson Imaging*. 2015;41(4):974-982.
  118. Marzi S, Piludu F, Sanguineti G, et al. The prediction of the treatment response of cervical nodes using intravoxel incoherent motion diffusion-weighted imaging [published online ahead of print 2017/06/19]. *Eur J Radiol*. 2017;92:93-102.
  119. Ding Y, Hazle JD, Mohamed ASR, et al. Intravoxel incoherent motion imaging kinetics during chemoradiotherapy for human papillomavirus-associated squamous cell carcinoma of the oropharynx: preliminary results from a prospective pilot study [published online ahead of print 2015/10/09]. *NMR Biomed*. 2015;28(12):1645-1654.
  120. Paudyal R, Oh JH, Riaz N, et al. Intravoxel incoherent motion diffusion-weighted MRI during chemoradiation therapy to characterize and monitor treatment response in human papillomavirus head and neck squamous cell carcinoma [published online ahead of print 2016/11/11]. *Journal of magnetic resonance imaging : JMRI*. 2017;45(4):1013-1023.

121. Salem A, Little RA, Latif A, et al. Oxygen-enhanced MRI Is Feasible, Repeatable, and Detects Radiotherapy-induced Change in Hypoxia in Xenograft Models and in Patients with Non-small Cell Lung Cancer [published online ahead of print 2019/05/06]. *Clin Cancer Res.* 2019;25(13):3818-3829.
122. Dubec MJ, Datta A, Little RA, et al. *First in-human technique translation of OE-MRI for hypoxia imaging onto an MR Linac system in patients with head and neck cancer.* <https://submissions.miramsmart.com/ISMRM2022/Itinerary/Files/PDF/Files/ViewAbstract.aspx>. Accessed June 13, 2022.
123. Marques JP, Kober T, Krueger G, van der Zwaag W, Van de Moortele PF, Gruetter R. MP2RAGE, a self bias-field corrected sequence for improved segmentation and T1-mapping at high field [published online ahead of print 2009/10/13]. *Neuroimage.* 2010;49(2):1271-1281.
124. Börjesson E, Palmér E, Sohlin M. *Optimization of MP2RAGE sequence parameters for head and neck T1-mapping and OE-MRI.* <https://gupea.ub.gu.se/bitstream/handle/2077/71546/Sja%cc%88lvsta%cc%88ndigt%20arbete%20Ellen%20ra%cc%88ttad.pdf?sequence=1&isAllowed=y2022>.
125. Bluemke E, Bulte D, Bertrand A, et al. Oxygen-enhanced MRI MOLLI T1 mapping during chemoradiotherapy in anal squamous cell carcinoma [published online ahead of print 2020/03/27]. *Clin Transl Radiat Oncol.* 2020;22:44-49.
126. Jezard P, Clare S. Sources of distortion in functional MRI data [published online ahead of print 1999/10/19]. *Hum Brain Mapp.* 1999;8(2-3):80-85.
127. Mikayama R, Yabuuchi H, Sonoda S, et al. Comparison of intravoxel incoherent motion diffusion-weighted imaging between turbo spin-echo and echo-planar imaging of the head and neck [published online ahead of print 2017/08/06]. *Eur Radiol.* 2018;28(1):316-324.
128. Aherne E, Chow K, Carr J. Cardiac T(1) mapping: Techniques and applications [published online ahead of print 2019/07/25]. *J Magn Reson Imaging.* 2020;51(5):1336-1356.
129. Chin S, Eccles CL, McWilliam A, et al. Magnetic resonance-guided radiation therapy: A review. *Journal of Medical Imaging and Radiation Oncology.* 2020;64(1):163-177.
130. Corradini S, Alongi F, Andratschke N, et al. MR-guidance in clinical reality: current treatment challenges and future perspectives [published online ahead of print 2019/06/07]. *Radiat Oncol.* 2019;14(1):92.
131. Kendall K, Mohamed AMM, Abdallah SRM, et al. Prospective quantitative quality assurance and deformation estimation of MRI-CT image registration in simulation of head and neck radiotherapy

- patients. *Clinical and Translational Radiation Oncology*. 2019;18:120-127.
132. Gunnlaugsson A, Persson E, Gustafsson C, et al. Target definition in radiotherapy of prostate cancer using magnetic resonance imaging only workflow [published online ahead of print 2019/03/20]. *Phys Imaging Radiat Oncol*. 2019;9:89-91.
133. Fujima N, Yoshida D, Sakashita T, et al. Intravoxel incoherent motion diffusion-weighted imaging in head and neck squamous cell carcinoma: assessment of perfusion-related parameters compared to dynamic contrast-enhanced MRI [published online ahead of print 2014/08/19]. *Magn Reson Imaging*. 2014;32(10):1206-1213.
134. Federau C. Intravoxel incoherent motion MRI as a means to measure in vivo perfusion: A review of the evidence [published online ahead of print 2017/09/09]. *NMR Biomed*. 2017;30(11).